Surface Characterization and New Tools for Research

R.St.C. Smart, W.M. Skinner, A.R. Gerson, J. Mielczarski, S. Chryssoulis, A.R. Pratt, R. Lastra, G.A. Hope, X. Wang, K. Fa, and J.D. Miller

INTRODUCTION

In the selective separation of mineral phases by flotation, surface chemistry is the principal determinant of the average contact angle for a specific mineral phase in a flotation pulp. The average contact angle is, in turn, the principal determinant of the bubble–particle attachment efficiency (E_a) in the overall collection efficiency (E_c) from which the flotation rate constant can be determined (Ralston 1994a). The recovery and selectivity in sulfide flotation is ultimately dependent on the relative rate constants of the different mineral phases. The average contact angle is not only mineral-specific, based on a statistical average of the mineral particles in that phase, but also the contact angle for each particle is an average of hydrophobic and hydrophilic areas across the particle surface. Determination of this hydrophobic/hydrophilic balance by particle therefore requires selection of the particular mineral phase. Obtaining this information is not necessarily a simple task in a flotation pulp containing many different mineral phases, different particle sizes of individual phases, adsorbed and precipitated species (often colloidal), and oxidized products. The hydrophobic/hydrophilic balance by particle and its statistical average by mineral phase require identification of the major species contributing to each category in surface layers (Smart, Jasieniak et al. 2003). In addition to adsorbed collector molecules and their oxidized products (e.g., dimers), hydrophobicity can be imparted to sulfide mineral surfaces by oxidation to produce polysulfide S_n^{2-} species resulting from loss of metal ions (usually Fe^{2+}) from surface layers. In acid solution, hydrophobic elemental sulfur can also be formed and is usually imaged in patches on the sulfide mineral surface (Smart, Amarantidis et al. 2003). Almost all other species found on sulfide mineral surfaces, such as oxide/oxyhydroxide/hydroxides, oxy-sulfur (e.g., sulfate), carbonate, hydrous silica, and fine gangue particles, are essentially hydrophilic but may be in the form of localized particles, colloids, and precipitates or continuous, reacted, or precipitated surface layers (Smart, Amarantidis et al. 2003).

The action of collector molecules in inducing hydrophobicity can be assisted by activating species such as copper and lead ions that complex the collector on the surface. Previous research has shown that this activation can be inadvertently produced by dissolution and transfer via solution of these ions to the surfaces of mineral phases not intended to float (e.g., Smart 1991; Lascelles and Finch 2002; Finkelstein 1997). Other complex mechanisms can affect both hydrophilic and hydrophobic contributions. They include, for instance

a. The extent of liberation of individual mineral phases by grinding or, conversely, the extent of remaining composite particles
b. Chemical alteration of the surface layers of sulfide minerals induced by oxidation reactions in the pulp solution

c. The presence of a wide range of particle sizes in the ground sulfide ores
d. Galvanic interactions between different sulfide minerals to produce different reaction products on the mineral surfaces
e. Chemical interaction between particles in the form of aggregates and flocs
f. The presence of colloidal precipitates arising from dissolution of the minerals, particularly sulfides, and grinding media
g. The mechanism of adsorption of reagents on specific surface sites
h. Competitive adsorption between oxidation products, conditioning reagents, and collector reagents

The primary purpose of surface characterization is, therefore, to identify these mechanisms with secondary application to the understanding and control of these mechanisms in plant practice.

This chapter summarizes some of the advances in surface analytical techniques and knowledge gained from surface characterization applied to flotation systems in the last two decades. There have been major additions to both the armory of instruments and the methodologies available for these studies. The selection of examples from both techniques and methods has been made as objectively as possible but necessarily has resulted in many excellent reports of research and plant surveys (or diagnoses) that have been missed or inadequately described. An attempt was not made to describe the theoretical or practical basis for each technique but, rather, the type of new information that it can provide. In compensation, reference is made to technique descriptions, reviews, and more complete reports in the references list. Some of the techniques surveyed in this chapter are now used in ore and plant surveys to provide part of the metallurgical information on which plant control is based but, more often, to diagnose reasons for losses in recovery or selectivity. Other techniques have been applied to basic studies of processes and mechanisms controlling flotation. Some case studies, combining information from different techniques, have been included to illustrate the now-established place of surface analysis and characterization in flotation research and practice.

X-RAY PHOTOELECTRON AND AUGER ELECTRON SPECTROSCOPIES

X-ray photoelectron and Auger electron spectroscopy techniques (Briggs and Seah 1992; O'Connor, Sexton, and Smart 2003), both analyzing the first 2–5 nm of the surface layers used in static (spot) and imaging modes, have produced primary information on processes b, c, e, f, and g previously described.

Sulfide Oxidation: Polysulfides

In sulfide flotation, the mechanisms of surface oxidation and the consequent physical and chemical forms of oxidation products on the surface, which are derived from studies using these surface analytical techniques, can be summarized as

- Metal-deficient (sulfur-rich) surfaces, polysulfides, and elemental sulfur
- Oxidized fine particles attached to larger sulfide particle surfaces
- Colloidal precipitates of metal hydroxide particles and flocs
- Continuous oxidized surface layers (e.g., oxide/hydroxide) of varying depth

- Adsorbed sulfate and carbonate species
- Nonuniform spatial distribution with different oxidation rates (e.g., isolated, patchwise oxidation sites; face specificity)

Scanning Auger microscopy (SAM) can provide both electron (secondary and backscattered) microscopic imaging for topography and phase identification together with surface elemental mapping, line scans, spot (submicron) analysis, and depth profiles. This type of information is illustrated in Figure 1 where a 50 wt % pyrite/50 wt % chalcopyrite mineral mixture was ground and conditioned in pH 9 nitrogen purged solution for >14 days. A very wide range of particle sizes is evident. Oxidized fine particles 0.1–10 μm are imaged, as well as flocs comprising clumps of loose aggregates with dimensions 1–3 μm, consisting of smaller spheroidal particles each with approximate diameters 0.1–0.5 μm. A similar range of particles is usually seen in samples taken from operating flotation plants. The flocs are not necessarily observed on similar surfaces that have been laboratory-conditioned for shorter periods (i.e., <1 hr) but have been seen in plant samples following fine grinding in which accelerated dissolution of pyrrhotite and iron grinding media has occurred. They have been precipitated from saturated ferric hydroxide solution as colloidal $Fe(OH)_3$ particles. Mechanical agitation or ultrasonication/decantation easily removes these flocs and some oxidized fine particles from the sulfide surfaces, showing that they are only weakly bonded to the oxidized sulfide minerals. The depth profiles for the oxygen signal in Figure 1c illustrate the variation in oxidized surface layers on different positions on the pyrite (left-hand side, upper particle) and chalcopyrite (right-hand side, underlying particle) from 5 to 80 nm. The >300-nm signal is from a ferric hydroxide floc. All of these surface species, which are typically in islands or reacted patches of the particle surface, contribute to hydrophobicity.

$$MS + xH_2O + \frac{1}{2}xO_2 \leftrightarrow M_{1-x}S + xM(OH)_2 \qquad \text{(EQ 1)}$$

It is now well established that iron-containing sulfide minerals (e.g., pyrite, pyrrhotite, chalcopyrite, pentlandite, arsenopyrite) essentially follow a reaction mechanism similar to that in Equation 1, in that iron hydroxide products and an underlying metal-deficient or sulfur-rich sulfide surface are formed. The seminal work of Buckley, Woods, and their colleagues, using a combination of X-ray photoelectron spectroscopy (XPS) and electrochemical techniques (reviewed in Smart, Amarantidis et al. 2003), has clearly demonstrated this mechanism in single mineral studies. In their work, oxidation of abraded pyrite surfaces exposed to air for a few minutes produced a high binding energy (BE) doublet component of the S 2p spectrum in addition to ferric oxide/hydroxide reaction products (Buckley and Woods 1987). The sulfur product was attributed to an iron-deficient $Fe_{1-x}S_2$ surface layer with the later proposition that polysulfide-like species S_n^{2-} are formed. Specifically, Mycroft et al. (1990) have correlated XPS and Raman spectra of electrochemically-oxidized pyrite surfaces with polysulfide model compounds but only at E_h > 600 mV, pH 5. Recently, monolayer-sensitive synchrotron radiation XPS (SRXPS) and time-of-flight secondary ion mass spectrometry (TOF-SIMS) (discussed in the following sections) have been used to verify the polysulfide formation in surface oxidation under plant conditions.

The importance of the S_n^{2-} n>2 polysulfides is that they contribute to hydrophobicity independently of collector addition. Collectorless flotation of pyrite in alkaline solution, correlated to electrochemical oxidation, can be explained by the production of a hydrophobic sulfur-rich surface together with hydrophilic iron hydroxide species (Ahlberg, Forssberg,

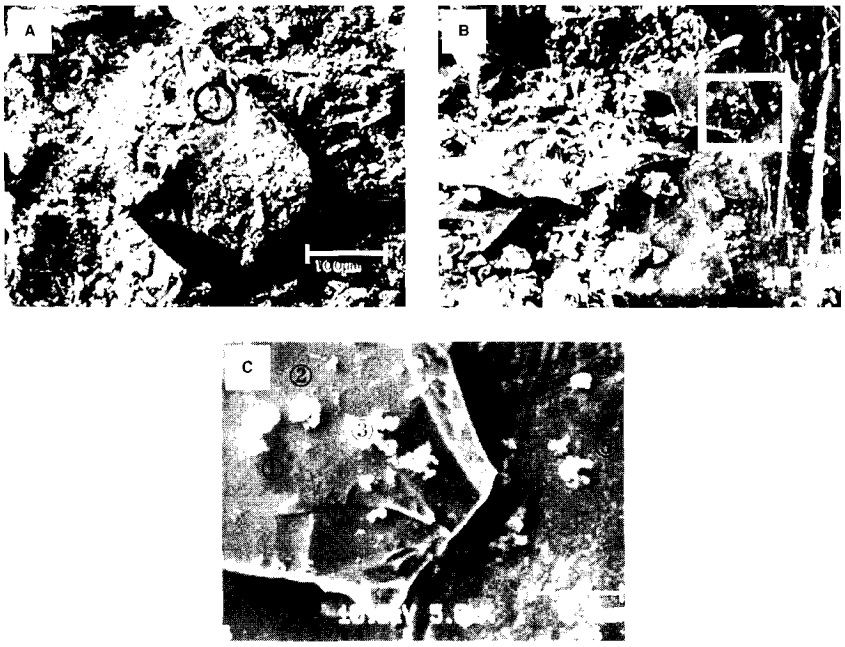

Source: Adapted from Smart, Amarantidis et al. 2003

FIGURE 1 SAM images from pyrite and chalcopyrite particles at successively higher magnifications (i.e., white bar = (a) 100 μm, (b) 10 μm, (c) 5 μm). Oxygen depth profiles for Auger analysis gave approximately 5, 30, >300 (pyrite particle), 80, and 10 nm (chalcopyrite particle), respectively, for each of the five points in (c).

and Wang 1990). After grinding, the surface becomes substantially covered by the hydrophilic species, and no significant flotation is observed without addition of collector. Collectorless flotation can, however, be easily obtained after complexing the iron with ethylenediamine tetraacetic acid (EDTA) in solution, indicating that the underlying hydrophobic sulfur-rich layer is responsible for pyrite flotation under these conditions. Elemental sulfur was not evident at pyrite surfaces exposed to air or neutral to alkaline solutions (Buckley and Woods 1987; Buckley, Hamilton, and Woods 1985). Thin layers of elemental sulfur were, however, observed on pyrite surfaces exposed to aerated, dilute sodium sulfide solutions (Buckley and Woods 1987; McCarron, Walter, and Buckley 1990). The collectorless flotation of chalcopyrite after air exposure or solution oxidation has been directly correlated with the surface composition determined by XPS (Zachwieja et al. 1989). Removal of iron hydroxide species during conditioning in alkaline solution to leave the hydrophobic sulfur-rich sulfide surface showed strong flotation. Conversely, oxidized chalcopyrite surfaces reduced in situ became copper deficient and were unfloatable.

A specific illustration of the XPS observation of polysulfide formation is found in galena oxidation in pH 9 solution from fresh fracture to 30-minutes aeration (Figure 2) (Smart et al. 2000). The growth of the high BE components of the sulfur S 2p spectra, due to S_n^{2-} species (B n=2; C n>3), is correlated with increasing contact angle and flotation recovery (Prestidge and Ralston 1995). The evidence for assignment of the high BE components of S 2p XPS spectra to metal-deficient, polysulfide defect sites and elemental sulfur has been reviewed (Smart, Skinner, and Gerson 1999).

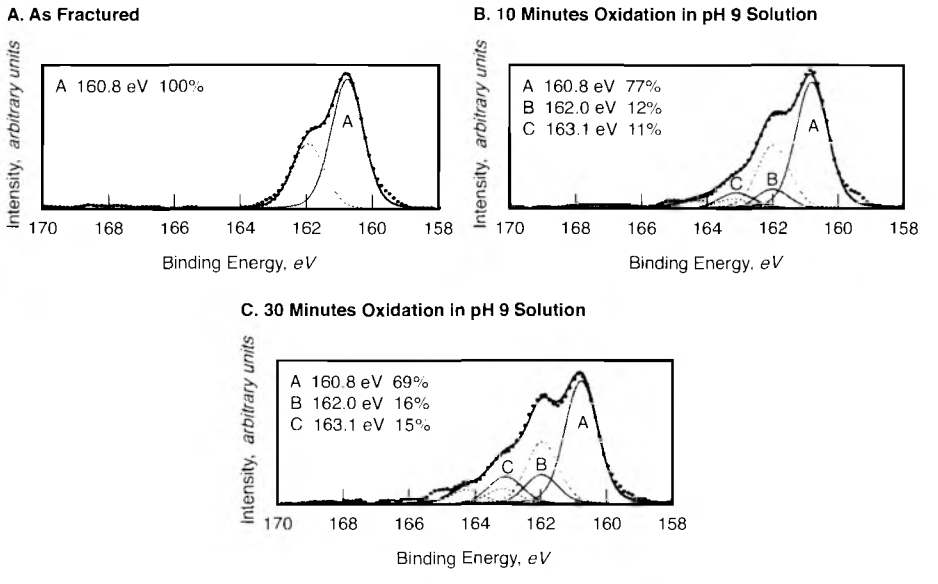

Source: Adapted from Smart et al. 2000.

FIGURE 2 XPS S 2p spectra from galena

Collector Actions

XPS and SAM have also done much to increase understanding of the actions of collector molecules in flotation, which are considerably more complex than the earliest simplistic model of adsorption of the head group and dangling hydrophobic tail. Their actions in several different modes have been studied using XPS and SAM in recent research (Smart, Amarantidis et al. 2003), namely

- Adsorption to specific surface sites
- Colloidal precipitation of metal–collector species from solution
- Detachment of oxidized fine sulfide particles from larger particle surfaces
- Detachment of colloidal metal oxide/hydroxide particles and flocs
- Removal of adsorbed, oxidized surface layers
- Inhibition of oxidation
- Aggregation and disaggregation of particles
- Patchwise or face-specific coverage

The presence of adsorbed xanthate on freshly fractured galena surfaces has been confirmed from both S 2p spectra and the more surface-sensitive X-ray induced Auger spectra (i.e., S LMM and Pb NOO) signals. The work of Buckley and Woods (1991) has correlated xanthate coverage (using voltammetry) with XPS spectra and flotation recovery showing that only a fraction of the monolayer is adsorbed at maximum recovery. Sub-monolayer, perpendicularly-oriented, adsorbed lead ethyl xanthate was confirmed in combined XPS, Fourier transform infrared (FTIR) spectroscopy, and controlled potential studies (Suoninen and Laajalehto 1993). There are now many examples of studies in the literature in which uptake of the collector molecules on the sulfide mineral surface occurs through the formation of colloidal (precipitated) metal-xanthate or metal-hydroxyxanthate species in solution

TABLE 1 Survey of the atomic concentrations (%) of elements for undeslimed pyrite particles conditioned at pH 4, N_2 purged

	Initial	Etch	Initial	Etch
Element	**[DCDTP] = 0 M**		**[DCDTP] = 7.5×10^{-3} M**	
Carbon (C)	28	7.8	26	8.3
Oxygen (O)	28	24	11	5.2
Iron (Fe)	10	27	21	39
Sulfur (S)	27	33	40	47
Calcium (Ca)	3.6	4.6	0.45	<0.05
Phosphorus (P)	0	0	0.28	0

or close to the surface. XPS and FTIR studies have shown that both copper(I) ethyl xanthate (XPS) and diethyl dixanthogen (FTIR) can be detected on the sphalerite surface as a result of reaction (Prestidge et al. 1994).

It is generally agreed that if sufficient hydrophilic oxidized material is present on the mineral surfaces, this will overcome any natural or self-induced floatability as well as modify the collector-induced floatability of the sulfide particles (e.g., Shannon and Trahar 1986). It has been suggested that collector molecules have the dual action of removing oxidized products from surfaces and providing a hydrophobic surface for bubble attachment and flotation. The surface cleaning action of xanthate has been reviewed by Senior and Trahar (1991) in studies of the flotation of chalcopyrite in the presence of metal hydroxides. The "cleaning" mechanism does not appear to be simple dissolution of the oxidized metals as can be achieved with other complexing agents (e.g., EDTA), because the amount of xanthate necessary to restore floatability is stoichiometrically orders of magnitude below that required for the complete conversion of the metal hydroxides to dissolved metal xanthate species. This fact is also well established in plant practice where EDTA additions are effective in giving increased recovery but are prohibitively expensive.

XPS indications of the cleaning action in removing oxidized surface layers were previously noted (Smart 1991), in which the initial high BE shoulder on the Cu 2p peaks, attributed to charged hydroxide species, had been removed by the action of the xanthate from a ground chalcopyrite sample. A similar action is found with the collector dicresyldithiophosphate (DCDTP) (van der Steldt, Skinner, and Grano 1993). Table 1 shows that the surface oxygen percentage is dramatically reduced (~40%) by addition of 7.5×10^{-5} M at pH 4 (maximum adsorption) to undeslimed pyrite particles. Removing the fine particles from the ground pyrite sample, by three successive ultrasonication/decantation steps with solution replacement, also showed that the majority of the material removed by the collector addition is in the form of fine particles rather than oxidized surface layers, as the level of surface oxygen concentration after fines removal (i.e., 13%) is similar to that after collector addition. After collector addition, both sulfate and ferric hydroxide signals are reduced in the XPS spectra and the contamination by calcium, present on the surface before collector addition, is also removed. There has clearly been a process in which oxidized fine particles are detached from the pyrite surface by the collector addition similar to that in mechanical removal of these fine particles.

SAM results (Smart, Amarantidis et al. 2003) have demonstrated that at high xanthate concentrations (i.e., 10^{-3} M), the formation of a surface layer, likely to consist of the oily, hydrophobic dixanthogen species, can inhibit oxidation of pyrite surfaces that would otherwise produce iron hydroxide oxidation products on the surface and in solution at lower

xanthate concentrations. These results bring in to question the intetpretation and relevance of mechanisms derived from studies at higher collector concentrations where the collector has been added in the grinding stage or early in the conditioning stage.

Fine/coarse particle interactions and aggregation have been studied for the copper activation of sphalerite and the effect of xanthate addition using correlated microflotation and on-line particle size distribution analysis coupled with surface analysis. Significant aggregation of <20-μm fine particles to 20–30-μm aggregates is already observed during initial conditioning at pH 5.5 and 8.5 during the first 20 minutes before any reagent addition. Addition of Cu(II) at pH 5.5 produces some development of larger aggregates, 100–120 μm, but flotation response of the fine particles remains poor. At pH 8.5, there is no evidence of the larger aggregates on copper addition and flotation recovery of the fine particles is similarly poor. Addition of xanthate at pH 5.5 dramatically increases the extent of aggregation >100 μm and flotation recovery (>95%), whereas at pH 8.5, only weak, larger aggregates appear to form, and the recovery does not increase to the same extent (i.e., 60%–80%). In the presence of coarser particles (38–75 μm) at pH 5.5 with Cu(II) addition alone, a very high percentage of the fine particles were recovered and a fine/coarse particle aggregation (i.e., "piggybacking") mechanism was confirmed by on-line particle size analysis and optical microscopy. At the higher pH 8.5, the interaction between fine and coarse sphalerite is slower and much less complete with correspondingly poorer flotation of both the fine and coarse fractions. XPS surface analysis confirms that this is due to partial coverage of the surface by colloidal hydroxides and overall hydrophilicity inhibiting strong hydrophobic interactions between the particles (Lange, Skinner, and Smart 1997).

There are now many case studies in which XPS surface analytical studies, combined with flotation metallurgy and solution chemistry, have directly contributed to improvements in flotation recovery and grade. For example, naturally floatable iron sulfides with graphitic surface layers have been identified and separately removed in copper flotation at Mount Isa, Australia (Grano, Ralston, and Smart 1990). This study also identified the selective removal of ferric hydroxides and carbonates by collector addition. The effects of fine grinding on flotation performance have been surveyed in a correlated XPS-flotation study (Frew et al. 1994) and specific application to the zinc regrind at Cominco Alaska's Red Dog mine has been reported (Frew, Smart, and Manlapig 1994). The action of an extended period of aerated conditioning before copper activation and collector conditioning in increasing sphalerite flotation at the Murchison Zinc (Australia) concentrator (Kristall et al. 1994) was explained, using XPS, by the removal of zinc hydroxides from the sphalerite surface and the concomitant appearance of a metal-deficient sphalerite surface. XPS also demonstrated an increase in the oxidation state of pyrite after aerated preconditioning. The presence of excessive surface oxidation in copper reflotation at Western Mining Corporation's Olympic Dam operation (Australia) (Smart and Judd 1994), identified by XPS analysis, led to improved operation of Lasta filters. A low flotation rate of galena in lead roughers at the Hilton Concentrator of Mount Isa Mines was analyzed (Grano et al. 1993, 1996) using XPS. The presence of precipitated species and their removal by a change of conditioning reagents (i.e., lime to soda ash) and collector reagent (i.e., ethyl xanthate to DCDTP, a collector that is stable in the presence of sulfite species over a wide pH range) has been used to address this problem.

SYNCHROTRON RADIATION XPS

Spectroscopic Advantages

Conventionally, obtaining a profile of composition as a function of depth requires either sequential ion beam sputtering and analysis, or the use of angle-resolved photoemission. Sputter profiling is limited because the disruption of chemical bonds beyond the top few monolayers in the surface detracts from any chemical environment information. Differential sputtering can also occur in compounds, resulting in a progressive enrichment of one constituent over another. Angle-resolved XPS can yield nondestructive, surface-sensitive information but requires flat surfaces and depth accuracy requires knowledge of photoelectron inelastic mean free paths in overlying reaction products. The majority of exposed sulfide mineral surfaces are not flat. Indeed, only a few sulfide minerals exhibit good cleavage planes (e.g., galena, sphalerite). It is also rare for the thickness distribution of reaction products to be uniform.

The XPS analysis depth can be modulated by controlling the kinetic energy and, hence, the escape depth of the emitted photoelectron of interest. This capability is afforded through the use synchrotron radiation. Current soft X-ray synchrotron beamlines offer high resolution monochromation in the 10–2,000 eV energy range with resolving powers in excess of 10^4 ($E/\Delta E$), and photon flux that is several orders of magnitude higher than conventional sources. Energy resolution and photon flux allow for full capability of the electron analyzer to be realized, giving superior photoelectron spectral line widths and excellent signal-to-noise ratio in short analysis times.

The universal curve of photoelectron escape depth as a function of kinetic energy is reproduced in Figure 3. The maximum surface sensitivity is attained when the kinetic

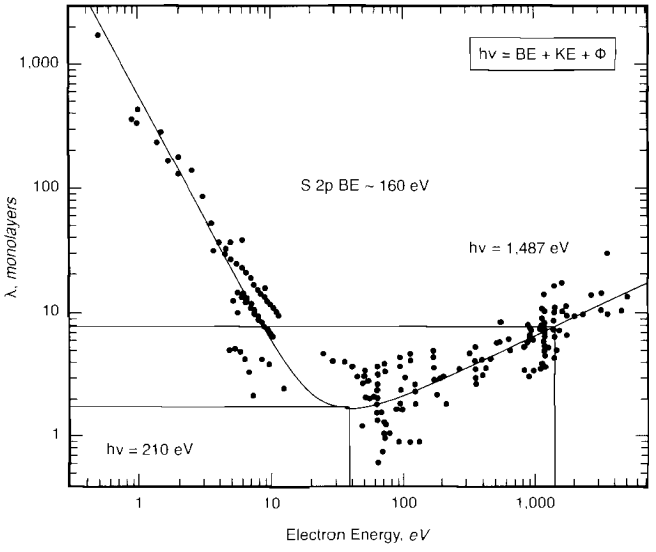

Source: Adapted from Carlson 1975.

FIGURE 3 Universal curve of photoelectron escape depth as a function of kinetic energy. Photoemission energy conservation equation shows the relationship between incident photon energy (hv), photoelectron BE, kinetic energy (KE), and instrumental work function (ϕ).

energy of the emitted photoelectron is in the range of 40–50 eV. To achieve this for the S 2p core-line (~160 eV BE), for example, an X-ray energy of approximately hν = 210 eV should be used. These conditions yield an almost fivefold enhancement in surface sensitivity over a conventional Al Kα source of hν = 1,487 eV for the S 2p signal.

Surface Sensitivity and Fracture Surfaces

The enhanced surface sensitivity and spectral resolution afforded by SRXPS is exemplified by the analysis of the fracture surface of pyrite (FeS_2). Figure 4a and 4b reproduce the S 2p core-line measured using a conventional monochromated Al Kα source (1,487 eV) and a synchrotron source (206 eV), respectively. The narrower line widths are immediately apparent in Figure 4(b). Two new S 2p doublet contributions (peaks a and b) appear to be located at lower BE relative to the main peak. These two new peaks in the pyrite S 2p spectrum are confirmed to derive from surface contributions as their intensities relative to the main peak (bulk peak) decrease with increasing excitation energy (Nesbitt et al. 1998). The interpretation of these surface core-level shifts requires consideration of the molecular orbitals involved in bonding, the mineral structure (e.g., metal and ligand coordination), and the fracture mechanism. A detailed description is not possible within the constraints of this review and the reader is directed to work by Nesbitt et al. (1998) for a comprehensive explanation. Put simply, during pyrite fracture, both Fe–S and S–S bonds may be ruptured. This results in a reduction in the coordination of metal and ligand (in this case, sulfur) sites at the surface and changes in electron density associated with these sites. Electrons involved in bonding are usually retained at the ligand (sulfur) site. The rupture of Fe–S bonds leaves the

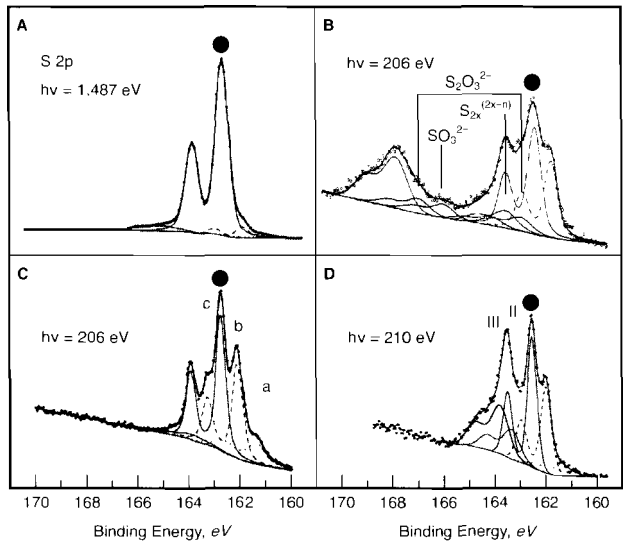

FIGURE 4 Sulfur 2p core-line spectra of fractured pyrite surfaces (a) using a conventional monochromated Al Kα source, and (b) a 206-eV synchrotron source (Schaufuss et al. 1998). Subsequently reacted pyrite surfaces are shown for (c) air oxidation for 14 hours (Schaufuss et al. 1998) and (d) adsorption of mercaptobenzothiazole from solution (Szargan, Schaufuss, and Rossbach 1999). The spectral contributions from bulk sulfur dimers (S_2^{2-}) are indicated by the solid circles (●) above the primary S $2p_{3/2}$ component.

surface sulfur dimer site with increased electron density and, hence, will emit photoelectrons of lower BE than the fully coordinated bulk sulfur dimer (peak b in Figure 4b). The formal oxidation state of the monomeric S^{1-} produced by S–S bond rupture reduces to S^{2-} through the associated oxidation of Fe^{2+} to Fe^{3+}, giving rise to even greater electron density associated with this site and hence an even lower BE (peak a) (Nesbitt et al. 1998). This level of detail is not possible using conventional, laboratory-based XPS instrumentation and the level of surface sensitivity afforded by SRXPS approaches that of static secondary ion mass spectrometry (static SIMS), as well as atomic force and scanning tunneling microscopies (AFM and STM) and low-energy electron diffraction. Moreover, nondestructive and quantitative surface- and bulk-sensitive measurements may be made in the same experiment, simply by varying the incident photon energy.

A range of important metal sulfide minerals has been examined by SRXPS over the last decade, looking at surface states and initial reactions. These include, for example, galena, PbS (Paulucci and Prince 1990; Leiro et al. 1998; Kartio et al. 1998); pyrite, FeS_2 (Bronold, Tomm, and Jaegermann 1994; Nesbitt et al. 1998; Schaufuss et al. 1998); marcasite, FeS_2 (Uhlig et al. 2001); pyrrhotite, $Fe_{1-x}S$; millerite, NiS (Nesbitt et al. 2001); arsenopyrite, FeAsS (Schaufuss et al. 2000); loellingite, $FeAs_2$ (Nesbitt, Uhlig, and Szargan 2002); gersdorfite, NiAsS (Nesbitt, Schaufuss et al. 2003); covellite, CuS; chalcocite, Cu_2S (Laajalehto et al. 1996); and chalcopyrite, $CuFeS_2$ (Harmer et al. 2004). This is by no means an exhaustive list; however, Harmer and Nesbitt (2004) have published a treatment of SRXPS interpretation showing how the sulfide mineral structure and composition determine whether surface reconstruction occurs as a result of fracture and the type of species exposed at the surface (e.g., metal oxidation, ligand polymerization). Recent work, combining *ab initio* calculations with spectroscopic analysis (von Oertzen, Skinner, and Nesbitt 2005), has confirmed this interpretation for pyrite, chalcopyrite, and molybdenite, MoS_2 (von Oertzen, Harmer, and Skinner, in press). This provides a high level of support for the synchrotron XPS interpretation of other important sulfide mineral fracture surfaces.

Surface Reaction

The implications of using these kinds of measurements for minerals processing are manifold as they enable the first surface exposed to solution to be probed (i.e., the fracture surface immediately exposed during grinding). The subsequent initial reactions at this surface may also be studied in depth using SRXPS in similar detail. Figures 4c and 4d illustrate further SRXPS examples of oxidation and collector adsorption at pyrite fracture surfaces. From these types of studies, it is possible to follow the relative reactivity of the various surface states exposed on fracture and, in turn, relate this reactivity back to the structure and bonding within the mineral.

Other Aspects of SRXPS

In the soft X-ray region, photoionization cross-sections can vary strongly with photon energy. This can be used to great advantage in SRXPS, particularly in valence band studies. By collecting the valence band spectrum of a mineral at several photon excitation energies, it is possible to enhance or diminish the spectral intensity contributions from metal and ligand bonding and nonbonding orbital, thereby identifying them and monitoring their involvement in surface reaction (Nesbitt et al. 2002; Nesbitt, Uhlig et al. 2003). Where possible within the constraints of surface roughness, angle-resolved measurements may also be performed to further enhance surface sensitivity, particularly for adsorbate studies.

SRXPS in conjunction with near-edge X-ray absorption fine structure (NEXAFS) spectroscopy provides an extremely powerful combination for the study of sulfide minerals (Goh, Buckley, Lamb, Skinner et al. 2006; Goh, Buckley, Lamb, Roseberg et al. 2006). NEXAFS yields information on metal and ligand coordination, oxidation state and relative location. It is particularly useful in monitoring organic reagent bonding mechanisms and molecular orientation at the mineral surface.

The Future

Much of the methodology for the study of fracture surfaces has now been established, despite the past scarcity of appropriate beamline/end-station combinations for these studies. Recent developments such as the soft X-ray facilities at the Canadian Light Source and the new Australian XPS/NEXAFS end station (initially located at the National Synchrotron Radiation Research Center in Taiwan) have expanded the available capabilities for such investigations. The investigation of the mechanisms of subsequent surface reaction will necessarily provide impetus into the future, together with further instrumental developments (e.g., imaging photoemission, effective charge neutralization for insulating minerals).

TIME OF FLIGHT SECONDARY ION MASS SPECTROMETRY

Diagnosis of the surface chemical factors playing a part in flotation separation of a value mineral phase requires measurement of the species that are statistically different between the concentrate and tail streams, together with an estimate (if possible) of the magnitude of the differences. The recently developed statistical methods, based on TOF-SIMS, have moved toward this ultimate aim. This technique used in static mode involves a very low flux of heavy ions impacting surface layers with mass spectrometric analysis of the secondary ions emitted from the surface. In the time of routine measurement, only 1–2 surface atoms in 1,000 are impacted. The secondary elemental and molecular fragment ions come from the first two molecular layers of the surface and provide a very detailed set of positive and negative mass fragments from simple ions (e.g., Na^+, OH^-) through to molecular ions of specific reagents (e.g., isobutyl xanthate $(CH_3)_2CHOCS_2^-$). Identification of molecular mass peaks for collectors, activators, depressants, precipitates, and adsorbed species is possible with comparative surface concentrations by particle and by phase between feed, concentrate, and tail streams.

The pioneering work of Nagaraj and Brinen (Brinen et al. 1993) with TOF-SIMS and the initial statistical analysis of air-dried particles using laser ionization mass spectrometry by Chryssoulis and colleagues (Chryssoulis, Reich, and Stowe 1992) have greatly contributed to the approaches described here. The improvements in the methodology include introduction of the mineral particles without exposure to air (Smart 1991), analysis of surface monolayer (or two), and full statistical analysis of all surface species. These analyses provide a statistical basis for assessment of surface chemical factors that have differentiated particles of a particular mineral phase that have reported to a concentrate from those that have reported to the tail.

Validation: Statistical Analysis

The use of TOF-SIMS to quantify changes in surface chemistry has been extensively validated in several ways. The amount of collector (e.g., xanthate, dithiophosphate) adsorbed from solution and monitored by UV adsorption was calibrated against the normalized

TOF-SIMS intensity for the molecular parent ion. A linear relationship up to monolayer coverage was found with a transition to a plateau for multilayer coverage due to the extreme surface sensitivity of the TOF-SIMS analysis (Piantadosi 2001). This is not a serious limitation because most minerals processing plant dosages are sub-monolayer. A second validation of the TOF-SIMS representation of the surface chemistry was conducted in comparison of spectra from polished surfaces of stoichiometric troilite, FeS; iron-deficient pyrrhotite, $Fe_{1-x}S$; and stoichiometric pyrite, FeS_2. The products of air oxidation of troilite and pyrrhotite have previously been shown to include disulfides and polysulfides (Smart, Amarantidis et al. 2003). The experiment was designed to test the representation of this surface chemistry in TOF-SIMS spectra. For the iron-sulfur fragments, the FeS_2/FeS ratios for troilite, pyrrhotite and pyrite were 0.59, 1.2, and 32, respectively. A similar sequence of S_n/S atomic fragment distributions confirmed the presence of polysulfides in these slightly reacted surface layers (Smart et al. 2000). Correlation of TOF-SIMS with XPS spectra (Figure 2) for freshly-cleaved galena (PbS) surfaces reacted in pH 9 solution for increasing periods of time has also shown a systematic increase in S_n/S ratios with increasing components of S 2p XPS spectra corresponding to polysulfide formation (Smart et al. 2000).

The basis for the methodology of sample preparation, mineral phase recognition, TOF-SIMS analysis, and statistical evaluation has been described in the paper by Piantadosi and Smart (2002). TOF-SIMS images of the particles in total ion yield mode are similar to those shown in Figure 5. Scanning for specific signals (e.g., Pb, Zn, Cu, Fe) can then be used to identify the particles of a specific mineral phase (e.g., galena, sphalerite, covellite, pyrite, chalcopyrite) for specific analysis. The region-of-interest (ROI) facility in the software allows definition of selected particles, as in Figure 5, corresponding to a specific mineral phase with the boundary for analysis set at a fixed position inside the contrast edge. When sufficient particles of the mineral phase have been identified for reliable statistics, a mass spectrum from each particle is recorded and stored. The statistical analysis (Piantadosi et al.

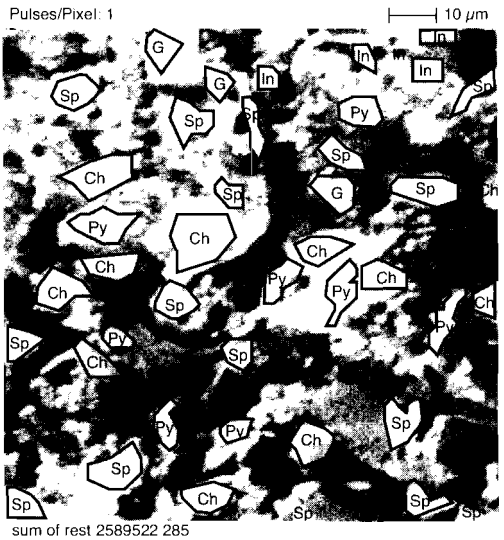

Source: Hart et al. 2004.

FIGURE 5 Principal component analysis identification of mineral phases: pyrite (Py), sphalerite (Sp), chalcopyrite (Ch), gangue materials (G), indium mounting material (In)

2000) then determines a mean value for each atomic and molecular species with 95% confidence intervals for each signal.

This analysis was first applied to the effects of calcium ion depression on galena flotation (Piantadosi et al. 2000). Correlation for 26 particle sets of Ca/Pb ratios for concentrate and tail streams gave 0.022 and 0.048, respectively, indicating that there is statistically more calcium (~2x) on galena particles surfaces in the tails compared with the concentrate. A second study (Piantadosi and Smart 2002) of the effect of iron hydroxides and collector, isobutyl xanthate (IBX), on galena flotation compared normalized intensities of IBX in feed, concentrate, and tail streams. There is a clear separation between particles of galena reporting to concentrate (0.005) and tail (0.001). The IBX concentrations on particles in the tail are not statistically different from those in the feed, due to increased hydrophilicity of galena particles in the tail rather than to reduced hydrophobicity. An early attempt to derive a hydrophobicity/hydrophilicity index, based on a ratio of signals from the (hydrophobic) collector (IBX) to (hydrophilic) oxy-sulfur products (SO_3) and iron hydroxide (FeOH), gave a value for the concentrate of 44.7 ± 13.7 compared with 7.1 ± 2.4 for the tail, but it is recognized that the index does not include all hydrophobic or all hydrophilic species contributing to the separation. Further comparisons for laboratory separation of galena and pyrite using di-isobutyl dithiophosphate (DIBDTP) collector have also been reported showing statistically ~12 times more collector on galena compared to pyrite. Galena particles reporting to the concentrate show statistically less calcium, lead hydroxide, and oxy-sulfur species on their surfaces compared to tail particles. The early flotation of galena was also considerably assisted by the presence of colloidal as well as adsorbed Pb DIBDTP.

Plant Diagnosis

This methodology has now been applied to full ore samples from plant operations including, as examples, Mount Isa Mines (MIM), Ok Tedi Mining Ltd. (OTML, Papua New Guinea), Falconbridge (Strathcona, Canada), Anglo Platinum (South Africa), Mineracao Caraiba (Brazil), and Inco Matte Concentrator (Sudbury, Ontario, Canada)—a total of 18 full statistical analyses to date (Smart, Jasieniak et al. 2003). Examples of results from samples supplied by the client from rougher and rougher scavenger flotation are shown in Figure 6. Poor flotation kinetics were exhibited by fine sphalerite (−10 μm) copper-activated down the rougher-scavenger banks. The study was designed to determine whether the poor flotation response to fine sphalerite was due to differences in mineral surface chemistry rather than hydrodynamic collision frequency factors alone. The process characteristics included pH 10.5 adjusted with lime, collector addition of IBX, and copper sulfate activation. Sphalerite particles in the −10-μm size range were selected using the ROI methodology so that the surface chemistry of this mineral phase was examined selectively. The bars in Figure 6 show the median value of each positive and negative ion signal with the 95% confidence intervals indicated by the smaller intervals at the top of each bar. Comparison between the rougher concentrate, scavenger concentrate, and scavenger tail eliminates all species for which confidence intervals overlap as not statistically significantly different (at least to the first level of statistical analysis). Other signals are clearly statistically different with dissimilar magnitudes in this comparison. In the selected positive ion species, discrimination into the concentrate streams is indicated for Zn, Cu, and Na with discrimination into the tail for increasing Fe, K, Si, Al, and particularly Mg. Low surface concentrations of Ca appear to favor the rougher concentrate but are apparently depressant into the scavenger concentrate and tail. In negative ion SIMS, the concentrates are statistically favored by high exposure of

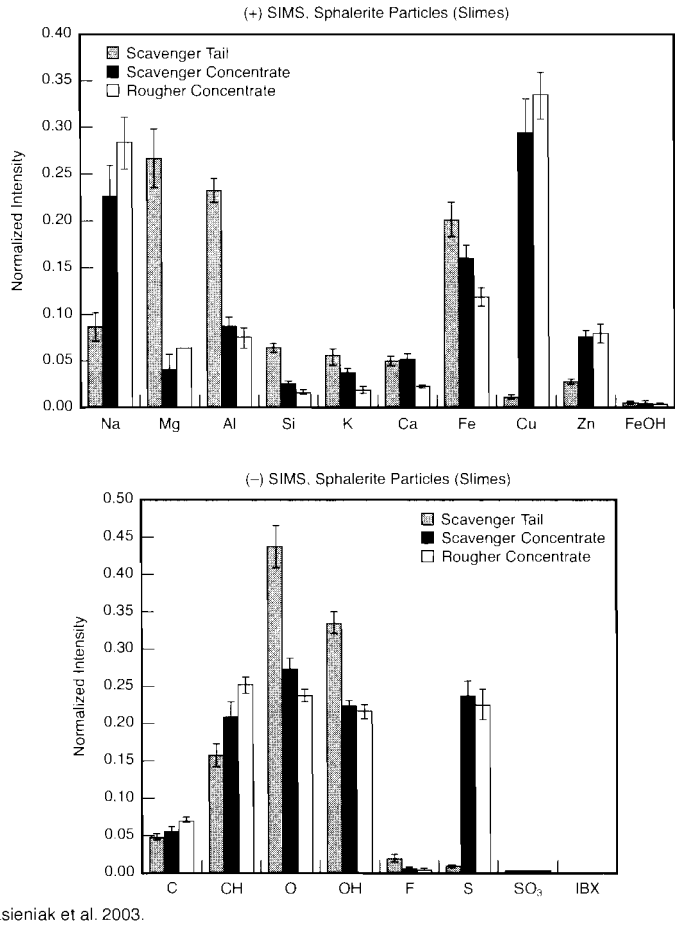

Source: Smart, Jasieniak et al. 2003.

FIGURE 6 Statistical TOF-SIMS spectra for sphalerite particles in the scavenger tail, scavenger concentrate, and rougher concentrate (bars = 95% confidence intervals)

S, CH, and by low surface exposure of F, OH, and O. More detailed examination of the collector IBX signal shows close correlation with the Cu signals. But the oxy-sulfur SO_3 signals are not statistically different between the three streams.

Comparisons show that the surface chemistry of the fine sphalerite is significantly different between concentrates and tails and even, for some species, between the rougher and scavenger concentrates. The most important difference is the absence of copper exposure and associated IBX on fine sphalerite in the tail stream, indicating low hydrophobicity of these particles. This difference is exaggerated by the presence of high concentrations of Mg, Ca, Al, OH, and F ions, apparently in the form of hydroxides and (alumino)silicates obscuring copper activation. Oxidation to oxy-sulfur species is not a major factor in the depression of fine sphalerite. Calcium ions, in particular, appear to have a depressant role between the rougher and scavenger flotation stages.

A second example of this statistical analysis for chalcopyrite in the OTML system has recently been published (Piantadosi, Pyke, and Smart 2001). It has been possible to estimate an average contact angle for this mineral phase by comparison with single mineral studies using the same collector.

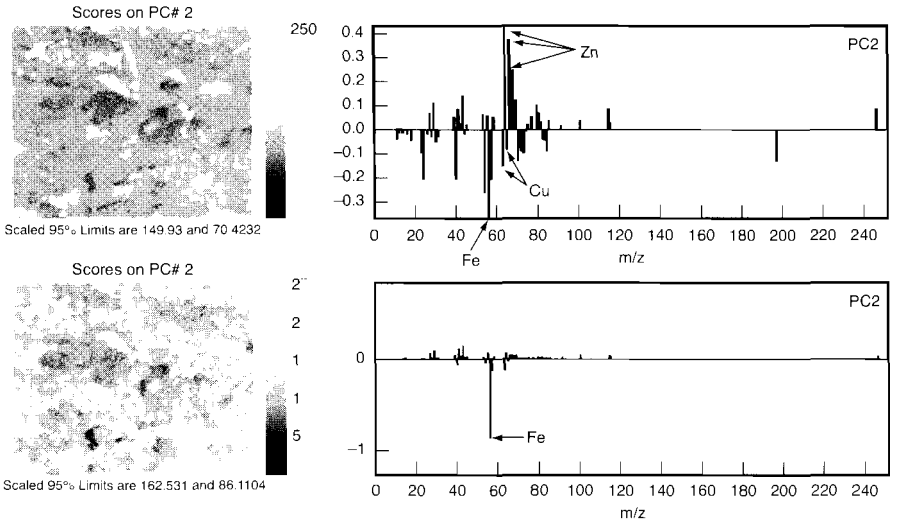

Source: Hart, Biesinger, and Smart 2006.

FIGURE 7 Second PC image scores and factor loadings for positive ion TOF-SIMS image data from the chalcopyrite/pyrite/sphalerite mixture. Top: autoscaled data; bottom: mean centered data. Images are 100 × 100 microns. Positive factor loadings appear bright in image; negative loadings appear dark.

Principal Component Analysis: Phase Recognition and Statistics

A recent improvement in the statistical analysis has been the introduction of principal component analysis (PCA) applied to the mass spectra. Reliable identification of specific mineral particles is central to this statistical analysis. A chalcopyrite/pyrite/sphalerite mineral mixture conditioned at pH 9 for 20 minutes to study transfer of Cu from chalcopyrite via solution to the other two mineral surfaces—because this mechanism can be responsible for their inadvertent flotation in copper recovery—showed no statistical difference in the copper intensities on pyrite and sphalerite (selected from Fe and Zn images) after this conditioning. PCA identifies combinations of factors strongly correlated (positively or negatively) in images or spectra from sets of data. In images, PCA selects these correlations from the mass spectra recorded at each of 256 × 256 pixels in a selected area of particles. In the image mode, PCA has proved to be a much better method of selecting particles by mineral phase with clearer definition of particle boundaries because of multivariable recognition. The first principal component, with factor loadings that are positive in weighting for all masses, is representative of the largest variance in the data set: topography and matrix (ion yield intensity) fluctuations. The second and subsequent principal components (PCs) will then have this variance removed and, as such, are topography- and matrix-corrected. Figure 7 illustrates the selection of sphalerite, chalcopyrite, and pyrite phases in the second PC from each of autoscaled and mean centered calculation modes. The transfer of copper ions from chalcopyrite dissolution to both pyrite (Smart 1991; Hart et al. 2004; Hart, Biesinger, and Smart 2006) and sphalerite surfaces (Finkelstein 1997) is confirmed by the surface analysis but it has also clearly separated a statistical difference in copper intensities between the sphalerite and pyrite phases in favor of sphalerite.

The PCA method has been applied to concentrate and tail samples collected from the Inco Matte Concentrator demonstrating extensive CuOH and NiOH transfer between the

chalcocite (Cc) and heazlewoodite (Hz) minerals (Hart et al. 2004). The PCs gave excellent recognition of the two mineral phases with reliable statistics on the regions selected. The close correspondence in these correlations between the isotopes of Cu (63, 65) and Ni (58, 60) gave further confidence in the interpretation. Statistical differences in normalized intensities (values are given in parentheses) illustrate the important discriminating depressant action of NiOH in flotation despite the activation of Hz by Cu transfer. The inadvertent flotation of Hz in the concentrate appears to be a result of Cu activation (0.16). There is also abundant Cu on Hz particles in the tails (0.08), but this is about half that in the concentrate. The Cu distribution between Cc and Hz particles in both concentrate and tails is the same within statistical 95% confidence intervals. The large statistical difference is in the Ni distribution where there is much more (~5×) hydrophilic Ni ions on Cc particles in the tail compared with the concentrate. Hence, Cc in tails appears to be the result of high depressant hydrophilic loadings rather than absence of hydrophobic Cu-collector surface species. The exposure of Cu on Cc particles in the tails as compared with concentrate is ~0.5, corresponding to an increase in Ni exposure of ~7.5. Both Cu activation of Hz and Ni depression of Cc are clearly operating in this system. There is also considerably more collector (>4×) on Cc particles in the concentrate than in the tails. In the tail samples, there is no statistical difference in intensity of the collector signals between Hz and Cc. The possible depressant action of Ca ions is not found to be selective in this surface analysis. Ca is found on both Cc and Hz surfaces in the concentrate and tails in statistically inseparable signals. The reduced chalcocite hydrophobic/hydrophilic ratio is, therefore, related to the presence of Ni ions on the surface, with a consequent reduction in bubble attachment efficiency. Hence, the statistical analysis can be used to confirm some mechanisms and deny others proposed to control recovery and selectivity, giving more focus on the control factors.

TIME OF FLIGHT LASER IONIZATION MASS SPECTROMETRY

Laser probe microanalysis combining laser excitation of small samples with a time-of-flight mass spectrometer dates back to the mid-1960s (Ruckman 1986). The application of the time-of-flight laser ionization mass spectrometry (TOF-LIMS) to analyze solid surfaces was introduced in 1986 by Clarke, Ruckman, and Davey. In 1988, while analyzing pyrite from the Brunswick Cu-Pb-Zn concentrator, it was accidentally discovered that free pyrite particles, devoid of galena inclusions, had significant levels of lead on their surfaces. The analyses showed that lead was confined to the surface and that it was more abundant on floated, as compared to rejected, free pyrites. Thus, the potential of TOF-LIMS to analyze the surface of mineral particles from plant samples in order to explain phenomena such as loss in selectivity during differential flotation, concentrate dilution, and rejection of free valuable minerals, was recognized. Comparative surface microanalysis by TOF-LIMS did become an integral part of several plant surveys but in most cases, this type of work is used for troubleshooting in (Cu)Pb-Zn, (Au)Cu, and platinum-group element (PGE) flotation plants (54 in total during the last 15 years).

Sample Preparation

Sample preparation for surface microanalysis with the laser microprobe was kept as simple as possible, on the premise that surface compositional differences and, in particular, their magnitude as opposed to absolute values, dictate the distinct response to flotation of otherwise similar particles. The only requirement is that all samples are treated in exactly the same way.

The sample preparation protocol requires cutting representative samples, filtering, followed by a brief rinse with deionized water to displace mill water, and then air drying. Cold storage in vials under a nitrogen atmosphere is encouraged for samples with readily oxidizable minerals (e.g., galena, pyrrhotite). Gravity separation by panning is used only when required to preconcentrate free particles of rare minerals, thereby facilitating picking under the stereoscope (e.g., gold, PGE minerals). Typically, 20 to 30 particles of the mineral of interest are picked from each sample or from two size fractions of the same sample when compositional differences between coarse and fine particles are being investigated.

Analysis

The commercially available laser microprobe instruments, the LIMA-2A, and its successor the PRISM, use Cassegrain optics, which permit specimen illumination and viewing, laser irradiation, and ion extraction—all normal to the sample surface (Figure 8). This unique feature is ideal for rough surfaces such as mineral particles because it minimizes topographic effects and increases elemental sensitivity. The use of a two-laser system (Figure 9) for the nonresonant multiphoton ionization (NR-MPI) of neutrals ablated by the laser microprobe technique (Schueler, Odom, and Evans 1986) allows for the decoupling of the sampling from the ionization step. This, in turn, enables an increase in surface sensitivity to the point where only copper is detected from a copper-activated sphalerite particle (i.e., monolayer detection), with a concurrent increase in elemental sensitivity (yielding minimum detection limits in the 1–50-ppm range (Figure 10). The analytical spot size (1 to 30 μm) and surface sensitivity (0.001 to 0.025) are inversely related to the degree of focusing and the power of the ablator laser. Laser probe microanalysis is very fast, with more than 100 analyses performed and processed per hour. Thus, large data sets, typically 200–400 strong, are collected and form the basis of t-test comparative statistical analysis, which is used to identify and rank activators and depressants (Bolin, Chryssoulis, and Martin 1997). Rotational factor analysis, a multivariate statistical analysis program, is used to validate t-test findings by analyzing data groupings based on factor loadings.

The TOF-LIMS technique in the NR-MPI mode is ideally suited for elemental surface microanalysis. In the single-laser negative ion mode, simple radicals (OH, CO_3, SO_3, SO_4, AsO_4, $FeOH_x$) associated with surface oxidation can be easily detected. Collector identification and loading measurements, although possible by TOF-LIMS (Chryssoulis et al. 1995), is preferably done by the complementary TOF-SIMS and vacuum UV surface analysis by laser ionization (VUV-SALI) techniques, as they are more sensitive for organic surface microanalysis because of better preservation of molecular ions (Chryssoulis, Weisener, and Dimov 1995).

The use of TOF-LIMS to quantify changes in surface composition has been extensively validated using several elements (e.g., Cu, Pb, Au, Ag) and minerals (e.g., pyrite, sphalerite, carbonaceous matter). Two examples are the linear relationship of TOF-LIMS data on surface Cu on sphalerite with the milligrams of Cu consumed, determined from solution assays (Chryssoulis, Kim, and Stowe 1994); and the surface concentration values of copper (in atomic %) measured by XPS (Stowe et al. 1993). Quantification of TOF-LIMS surface data is possible using minerals loaded to different degrees with the element of interest or with the help of relative sensitivity factors determined under standardized conditions (Dimov and Chryssoulis 1997). Surface characterization by TOF-LIMS and, in fact, any other surface microanalytical technique, is usually not a standalone investigation. In most cases, it is a followup investigation on a liberation study, which identified liberated minerals of readily

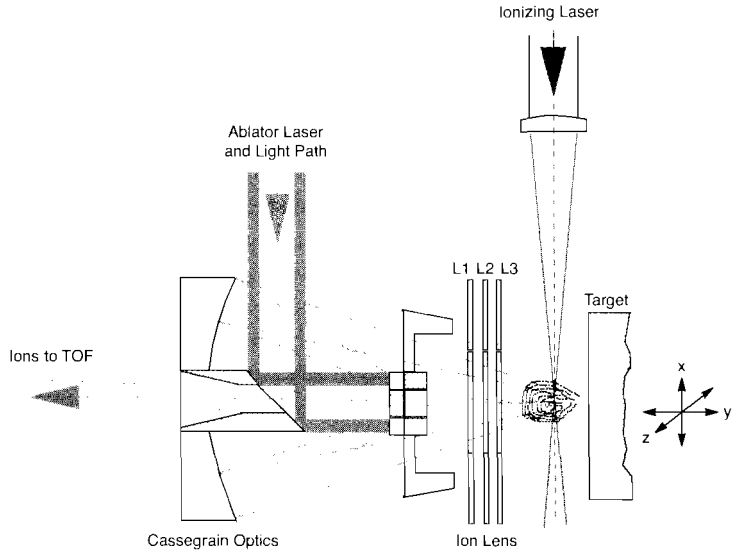

FIGURE 8 Schematic of TOF-LIMS sample analysis region

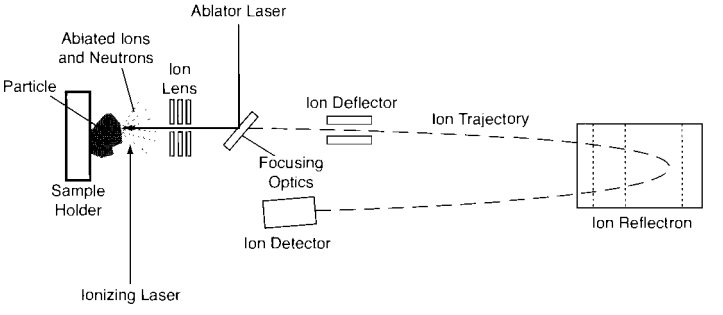

FIGURE 9 TOF-LIMS principle of operation

floatable size classes to be a significant fraction of losses to tails or a concentrate grade loss or misplacement to the wrong concentrate. Several case studies are discussed in the follow sections to illustrate this point.

Brunswick Cu-Pb-Zn Concentrator

In the Brunswick Cu-Pb-Zn concentrator (British Columbia, Canada), two long-standing issues have been the premature flotation of sphalerite in the primary Cu-Pb circuit, culminating in the production of a bulk Zn-Pb concentrate (Figure 11) and the dilution of the final Zn concentrate by pyrite. Several detailed liberation studies on extensive plant surveys documented that floated free particles are a significant part of both issues. TOF-LIMS studies did consistently show, firstly, significant amounts of Pb on the surfaces of the sphalerite and pyrite particles and, secondly, that this Pb had a major effect on the flotation of both minerals (Kim, Chryssoulis, and Stowe 1995). The surfaces of sphalerite and pyrite from competent run-of-mine (lump-size ore from the semiautogenous-grinding-mill feed) are clean of surface contaminants in contrast to conveyor belt fines (<100 μm), which are

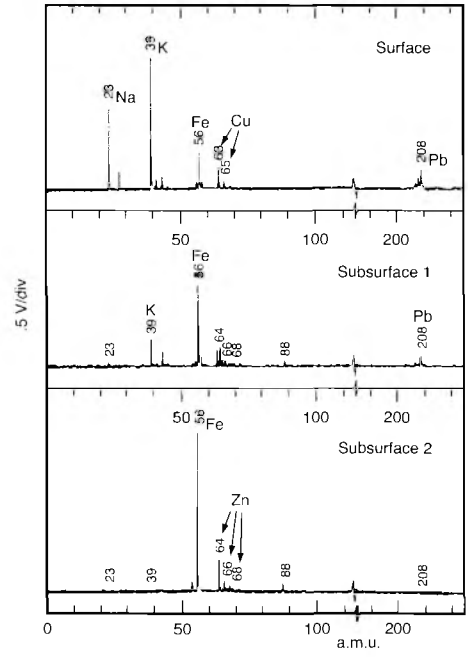

FIGURE 10 Successive TOF-LIMS spectra obtained from the uppermost surface layers of Cu-activated sphalerite grain by firing the ablator laser at the same site three times

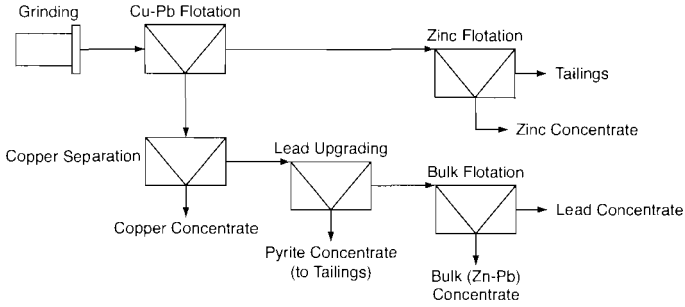

FIGURE 11 Brunswick mill flowsheet

inadvertently activated. Pre-activation by lead ions originating from galena begins as soon as the minerals are contacted with water (Kim, Chryssoulis, and Stowe 1995). Most of the lead-activated sphalerite and pyrite that floated in the primary Cu-Pb circuit followed galena to the Cu-Pb concentrate separation circuit. On the other hand, the lead-activated pyrite and sphalerite that was successfully removed in the Cu-Pb cleaners refloated in the zinc roughers. The presence of lead on sphalerite surfaces complicated activation by copper for zinc flotation, while sphalerite activated solely by lead was selectively rejected in the zinc cleaners as a result of the lime conditioning. Enlightened by these studies and following successful pilot-plant testing, galena flash flotation was introduced in 1998 with remarkable results both in the Cu-Pb and Zn circuits.

Probably the most important family of flotation chemicals is pH modifiers. A plant study of zinc rougher flotation at Brunswick was conducted using lime, soda ash, and a combination of both as the pH modifiers in order to establish the effects on sphalerite and pyrite flotation kinetics and on mineral selectivity. TOF-LIMS surface microanalysis was one of several microbeam techniques used in the investigation. The results revealed the important role of carbonate ion (from the soda ash) in cleaning and more specifically in removing lead from the sphalerite surfaces for effective activation by copper sulfate. The clear advantage of the soda ash–lime combination was to maintain the benefit of the additional Cu activation on sphalerite while at the same time increasing the effectiveness of the depressing action of Ca on the pyrite by increasing coverage (Nesset et al. 2001). The Brunswick concentrator now uses both soda ash and lime in their zinc circuit. The sequence of the soda ash, copper sulfate, and lime additions can be important, because Ca may be blocking sites for Cu sorption on pyrite. Ca is added after Cu (Kim et al. 1997).

Boliden Cu-Pb-Zn Concentrator

When treating Petiknäs South ore at the Boliden concentrator (Sweden), pyrite floating to the Cu-Pb rougher concentrate is largely liberated and is most abundant in the highly floatable 20–40-μm size range, indicative of true flotation. TOF-LIMS analysis revealed that its flotation could in part be ascribed to a plethora of activating ions such as Cu and Pb on the particle surfaces, together with a relative scarcity of depressant ions such as Ca and Fe. Several conditions were investigated in the laboratory with the intent of reducing the surface activators while enhancing the surfaces with depressants. Of these, only the synergistic use of lime and ferric sulfate showed any promise, and initial flotation tests have shown that these may indeed control pyrite flotation (Bolin, Chryssoulis, and Martin 1997).

Fine Sulfide Particles

TOF-LIMS, because of its tiny 1–3-μm analytical spot size, was used in two cases to identify differences in surface composition between coarser (>20 μm) and fine (<5 μm) particles of pentlandite from Inco's Clarabelle mill (Canada) (Chryssoulis et al. 1991) and of galena from MIM's lead-zinc mill that could be partly responsible for the slower flotation kinetics of the finer particles. In both cases, depressants were found in higher concentration on the finer particles.

Gold Flotation

Free gold particles of floatable size classes (7–150 μm) in general account for <10% of the gold losses in final flotation tails (Chryssoulis, Dunne, and Coetzee 2004). Evidently, surface modifiers played a role in their rejection. Comparative statistical analysis of TOF-LIMS data on floated versus rejected free gold from 10 flotation plants found that surface compositional changes compromised gold floatability in a number of ways (Figure 12). Excessive sorption of hydroxyl and calcium ions has been the most common cause for free gold rejection; this mostly occurring in the cleaner circuit. Ramping up the pH in the cleaners is one way to moderate this detrimental effect, another being supplementary addition of collector in the regrind at modest dosages.

The concentrator at Los Pelambres is a good example of a process where surface characterization of free gold particles by TOF-LIMS fostered an increase in gold recovery. The porphyry copper ore assaying 1.0% Cu, 0.02% Mo, with 0.03–0.05g Au/t, is processed using a standard Cu-Mo flotation circuit at a rate of 180,000 tpd. Gold deportments on 12-hour

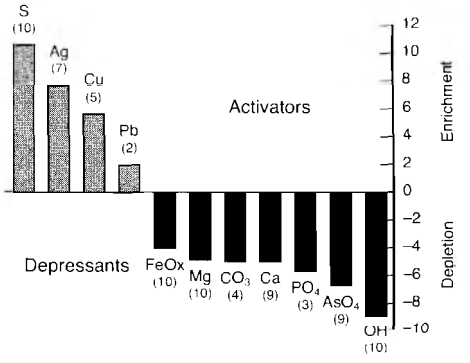

FIGURE 12 Ranking of inorganic surface modifiers affecting gold floatability, based on comparative analysis of floated and rejected free native gold and electrum particles from the concentrators. Numbers in parentheses give frequency of occurrence.

composite samples of the rougher and cleaner scavenger tails assaying 0.010 and 0.021g Au/t, respectively, established that approximately one-third of the gold losses were in the form of free gold particles in floatable size classes. Comparative surface microanalysis of floated and rejected free gold particles revealed that the surfaces of rejected gold grains had systematically less sulfur and silver, though they were enriched in lead and iron oxyhydroxides (Chryssoulis 2001). Based on these findings, a short flotation program was designed to evaluate two reagents: NaHS and 3418A. Sodium hyposulfite was chosen to convert lead carbonate on the surface of rejected free gold grains to sulfide, whereas 3418A is known to be an excellent galena and silver mineral collector. Following plant trials at modest dosages, 20g/t NaHS and 0.5g/t 3418A, overall gold recovery was improved by 7 percentage points.

The last example illustrates the complementary use of microscopy and detailed inorganic/organic surface microanalysis to characterize the factors that control the flotation kinetics of free gold. Surface microanalysis of equant and large flaky gold particles from concentrates of staged rougher flotation tests on a pyritic free milling gold ore determined progressively lower concentrations of the collector monomer on gold from each followup concentrate. Microanalysis also revealed a direct proportionality between the surface concentration of silver and the collector monomer (Figure 13). These two observations confirm that silver activates gold flotation and that collector monomers play a significant, previously not fully recognized, role in gold flotation. It was also determined that large gold flakes require four times as much collector in order to float at the same rate as equant gold grains.

INFRARED SPECTROSCOPY

Selective separation of mineral components is achieved by addition of specific collectors, activators, depressants, or modifiers and manipulation of solution conditions (i.e., pH, Eh, aeration). All these changes in solution composition are performed to make the valuable mineral components very hydrophobic, whereas gangue components should remain hydrophilic. The flotation behavior of ore components depends on the nature and structure of the surface hydrophobic or hydrophilic species produced. The possibility of monitoring surface phenomena at molecular and atomic levels at the interfaces of natural minerals contacted

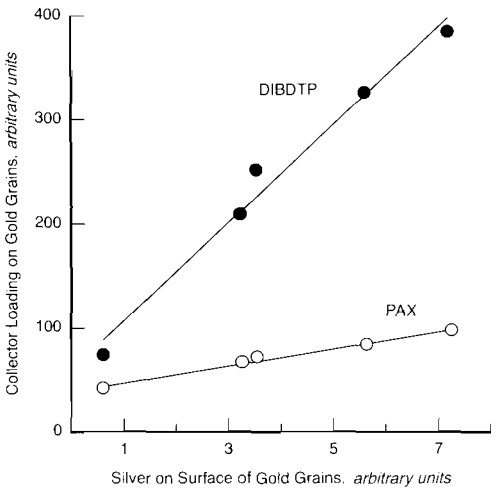

FIGURE 13 Correlation of DIBDTP and potassium amyl xanthate (PAX) loadings with surface concentration of silver (all in arbitrary units) on gold grains from sequential concentrates C1–C5 of a staged rougher test. DIBDTP (1 g/t) and PAX (12 g/t) were added in the mill.

with aqueous solution is vitally important for the understanding of the surface phenomena that govern selective and efficient flotation. This requires application of the appropriate experimental techniques.

Infrared spectroscopy is particularly well suited to determine the surface composition of minerals with adsorbed collectors at a molecular level. Infrared absorption is functional group selective, so it is particularly well adapted to detect small changes of the molecular microenvironment properties emerging at the interfaces. Experiments can be performed in situ at both gas–mineral and aqueous solution–mineral interfaces. There is only very gentle interaction of the infrared beam with the sample examined to ensure nondestructive analysis.

Infrared External Reflection Technique

In recent years, an infrared external reflection technique was developed (J.A. Mielczarski and Yoon 1989; J.A. Mielczarski 1993; J.A. Mielczarski and Mielczarski 1995, 1999; E. Mielczarski, Duval, and Mielczarski 2002) that offers the ability to overcome experimental problems and collect reliable data to monitor and understand surface phenomena at any mineral interface at a molecular level in close-to-real flotation conditions. The variety, precision, and reliability of information about interface phenomena delivered by this technique are superior to any other single technique.

The developed technique is based on specific interaction of electromagnetic waves with a multilayer system. A schematic diagram for a simple three-phase system is presented in Figure 14. For polarization perpendicular to the plane of the incident beam (s-polarization), there is only one electric vector, $E_{\perp Y}$, parallel to the substrate plane. Hence, only molecular groups of the adsorbed species with a dipole transition moment parallel to the interface in y direction can interact with the incident radiation and produce an absorbance band, $A_{\perp Y}$. For example, in the case of the adsorption of xanthate molecule involving both sulfur atoms with the same distance from interface (Figure 14), it is expected that the absorbance, $A_{\perp Y}$, will show the highest value. No interaction and, obviously, no absorbance band are observed

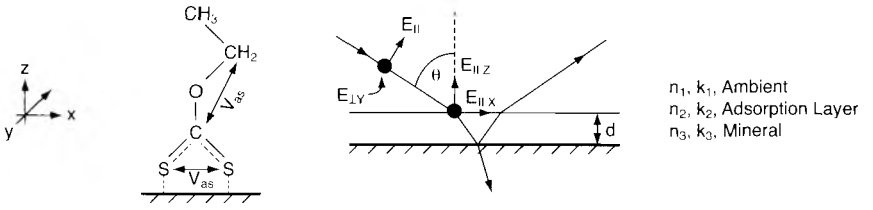

FIGURE 14 Schematic diagram of the interaction of electric field vectors in three directions with a simple three-phase system. Also shown is a xanthate molecule with dipole transition moments shown for the asymmetric stretching vibrations of the SCS group (parallel to interface) and of the asymmetric stretching vibrations of the COC group (almost vertical to interface).

when the sulfur-carbon-sulfur (SCS) group is turned 90° from the position presented in Figure 14, and the dipole transition moment of the asymmetric vibration of the SCS group becomes vertical to interface. For parallel polarization (p-polarization), there are two electric field vector components at the interface: one parallel, E_{IIX}, and one perpendicular, E_{IIZ}, to the substrate plane. Using the example of xanthate molecules at the surface presented in Figure 14, two absorbance bands—the A_{IIX} for the SCS vibration group and the A_{IIZ} related to the carbon-oxygen-carbon (COC) group vibration—will be present in the recorded spectrum. It is also possible to distinguish these two components because they show reverse absorbance; the first one produces negative absorbance, and the second one is positive.

The incident infrared beam reflected from a mineral surface carries all the information about surface composition and structure. With proper manipulation of the experimental optical conditions (incident angle and polarization), it is sufficient to record three spectra, which together give a three-dimensional "picture" of the species present at the mineral surface. Importantly, simulation of the adsorbed layer is carried out before any experiment is performed, allowing prediction of the best experimental conditions that give optimal spectral sensitivity and the maximum confidence in the interpretation of experimental results. This also significantly speeds up the experimental procedure.

The developed technique has unique properties compared with other known infrared techniques, such as transmission, diffuse reflectance, attenuated total reflection, and photoacoustic spectroscopies. This technique, supported by spectral simulation, allows almost all the details about the mineral–aqueous solution interactions to be obtained, including the

- Nature of the adsorbed products, and by which molecular group adsorption takes place
- Adsorbed quantities of different surface products (starting from 20% of monolayer)
- Surface distribution of the adsorbed species (uniform layer or patches with determined thickness)
- Molecular orientation of the adsorbed species (through orientation of particular functional groups)
- Molecular recognition (selective adsorption on specific surface sites)
- Lateral interaction between the adsorbed collector molecules
- Dynamic phenomena, such as kinetics of adsorption/desorption, stability of surface products, and surface mobility of the adsorbed species

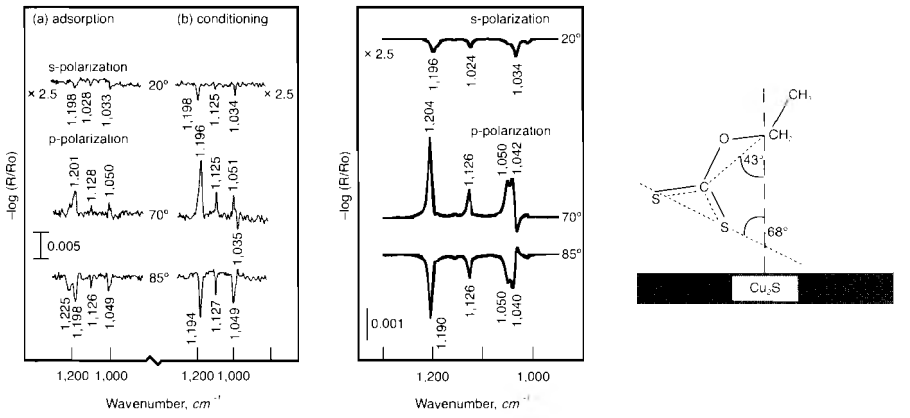

FIGURE 15 Results of infrared external reflection technique: (left) reflection spectra of xanthate on chalcocite, solution of 5 × 10^{-5} M and pH 9.2: (a) after 3 minutes of adsorption and (b) after 30 minutes of conditioning; (center) simulated reflection spectra of an isotropic 1-nm layer for different polarization and incident angles; (right) determined molecular arrangement of xanthate on chalcocite surface after conditioning.

This information leads to the determination of the mechanisms and dynamics of surface phenomena, which allow the design of selective and efficient flotation, and control of this process.

The developed infrared external reflection technique allows the unique ability for study of interface phenomena at a molecular level on heterogeneous substrates such as natural minerals. There is no limit; all types of mineral samples can be investigated. The experiments are fast and nondestructive. High sensitivity, in-situ-collected information in a multiphase system, including the region of strong absorption of substrate, makes this technique a very valuable experimental tool. The complexity of the recorded reflection spectra, their sensitivity to any variations of the optical properties of all bulk and surface components, and their spatial distribution in the system under investigation are, in fact, the major strengths of the technique.

Examples of results are presented in Figure 15. Experimental spectra recorded at three angles of incident beam and p-polarization (Figure 15, left) are compared with simulated spectra (Figure 15, center), and the similarity and differences (for example at about 1,040 cm^{-1}) indicate that the hydrophobic product is cuprous xanthate; that the adsorbed molecules are at first randomly oriented (Figure 15, left); and that after conditioning, they reorganize themselves in an oriented layer (Figure 15, center) with the molecular arrangement presented in Figure 15 (right) (J.A. Mielczarski et al. 1995) These results clearly explain the increase in hydrophobicity during conditioning and rationalize the conditioning procedure.

Another application is the monitoring and interpretation of the galvanic effect between two or more grains of different minerals. The detected changes are dramatic—from no adsorption to several monolayers of collector coverage formation, with major consequences for pyrite depression and galena flotation when they are together in collision in flotation pulp. However, if these two minerals are separately contacted with xanthate solution, pyrite is more hydrophobic than galena (Figure 16). These results clearly indicate that the observations and conclusions about the collector action—hence, also the surface hydrophobization—when

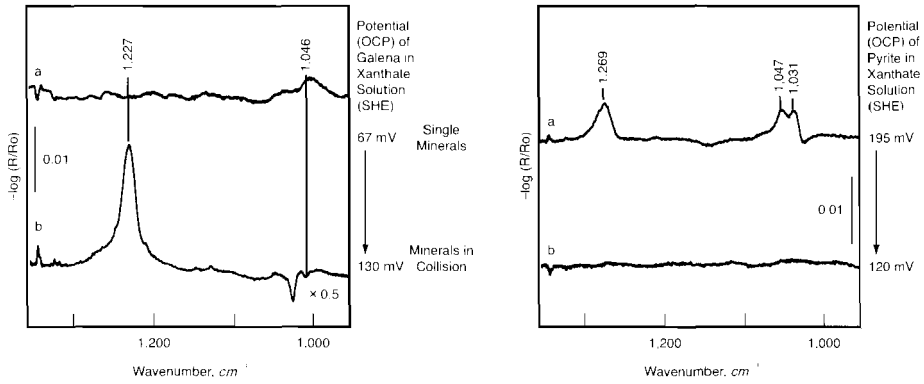

Source: E. Mielczarski and Mielczarski 2003a.

FIGURE 16 Reflection spectra of galena and pyrite after contact with amyl xanthate solution: (a) single minerals; (b) minerals in galvanic contact by collision. Open circuit potential (OCP) is reported vs. saturated hydrogen electrode (SHE).

made for single mineral systems do not describe the real situation in a multicomponent mineral system such as that in flotation pulp.

Numerous fundamental and practical questions have been answered with the help of this technique. This multidiagnostic technique has been applied extensively to the study of interaction of different sulfide minerals with various aqueous solutions including chalcocite (J.A. Mielczarski et al. 1995; J.A. Mielczarski, Xu, and Cases 1996), chalcopyrite (J.A. Mielczarski et al. 1995; J.A. Mielczarski, Mielczarski, and Cases 1997, 1998), tenantite, tetrahedrite (J.A. Mielczarski et al. 1995; J.A. Mielczarski, Mielczarski, and Cases 1997), galena, and pyrite (E. Mielczarski and Mielczarski 2003a, b). The collectors investigated were different xanthates, carbaminates, and phosphates. Major achievements are as follows:

1. Detailed description of solution conditions to produce selectively hydrophobic mineral surfaces,
2. Observation of strong interactions between different minerals in multicomponent systems and their influence on selective flotation,
3. Explanation of the role of particular reagents in the flotation system and the best surface modification conditions, and
4. Understanding of the difference in hydrophobization action between different xanthate-type collectors.

This information has allowed important full-industrial-scale technological improvements to be proposed that have already brought benefits to the user (e.g., J.A. Mielczarski et al. 1999). Similarly, extensive research has been performed on selective hydrophobization of semisoluble minerals such as fluorite (E. Mielczarski, Mielczarski, and Cases 1998; J.A. Mielczarski, Mielczarski, and Cases 1999; E. Mielczarski et al. 2002), apatite (J.A. Mielczarski and Mielczarski 1995), calcite (J.A. Mielczarski and Mielczarski 1999), quartz (J.A. Mielczarski et al. 1995), and oxides (E. Mielczarski et al. 2004). A more general description of the applications of infrared external reflection techniques focused on the understanding and modification of surface phenomena (hydrophobicity) can be found in recent papers (E. Mielczarski and Mielczarski 2003b, 2005).

FIGURE 17 Internal reflection configurations: (a) with mineral particles deposited on transparent reflection element, and (b) with adsorbed layer on reflection element made of transparent mineral

Infrared Internal Reflection Spectroscopy

Another infrared reflection technique, which ensures a better understanding of mineral surface phenomena that govern selective flotation, is internal reflection spectroscopy (IRS), also known as the attenuated total reflection (ATR) technique. Two experimental approaches have been explored. In the first approach, the mineral grains in contact with solution are in close vicinity to the ATR element (Figure 17a). In this case, a reflection spectrum of the outermost mineral surface layer could be recorded. In the second configuration, the investigated adsorption layer is produced directly on a reflection element made of natural or synthetic mineral (Figure 17b). The adsorption layer is also in contact with aqueous solution during measurement.

The latter approach is limited to the minerals that are transparent for infrared radiation, such as fluorite (CaF_2), sphalerite (ZnS), and so forth. The first approach can be used for any type of mineral grains. Some examples of mineral grain surface characterization could be found in reports by Mielczarski and colleagues (J.A. Mielczarski 1986; J.A. Mielczarski, Nowak, and Strojek 1980, 1983; Leppinen and Mielczarski 1986). The recorded in-situ spectra carry the information about mineral surface composition and relative amounts of the determined surface species. The second approach is described in more detail in the following paragraphs.

In-situ quantitative measurements of interfacial phenomena, such as surfactant adsorption at mineral surfaces using FTIR/IRS, have been achieved in the last two decades (Sperline, Muralidharan, and Freiser 1987; Jang and Miller 1993; Fa and Miller 2003; Kellar, Cross, and Miller 1989). The results of these quantitative measurements greatly improved the understanding of surfactant adsorption at various surfaces. The basic experimental setup for FTIR/IRS sampling is shown in Figure 18. In the sampling region, three optically distinct phases are distinguished by their different refractive indices, n_i, and absorption coefficients, k_i, where i = 1, 2, 3 (Figure 18, left). The infrared (IR) light enters the interfacial region from a dense phase (refractive index n_1) to a rare phase, n_3 ($n_1 > n_3$). The interfacial region to be probed is the second phase (n_2) sandwiched in between the first (incident) phase and the third phase. When the incident angle is larger than the critical angle $\theta_c = \sin^{-1}(n_3/n_1)$, total internal reflection occurs, and an evanescent optical field is generated in phase 3 (Figure 18, right). The guided IR light inside the infrared element (IRE) experiences multiple reflections at both sides of the IRE crystal. This ensures a high signal-to-noise ratio that is important for quantitative analysis of adsorption reactions.

The simplest quantitative measurement is a comparison of the spectra of unknown samples with those of known samples. The molecular packing angle (Simon-Kutscher, Gericke, and Huhnerfuss 1996; Jang and Miller 1995), adsorption density (Jang and Miller 1993; Jang and Miller 1995; Tejedor-Tejedor and Anderson 1990), and film optical constants (Sperline, Muralidharan, and Freiser 1987; Jang and Miller 1993; Fa and Miller 2003;

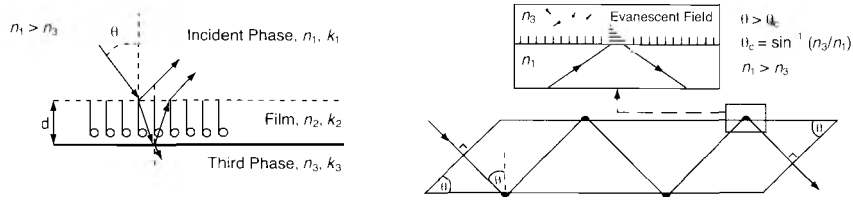

FIGURE 18 Typical FTIR/IRS experimental setup

Kellar, Cross, and Miller 1989; Simon-Kutscher, Gericke, and Huhnerfuss 1996; Jang and Miller 1995; Tejedor-Tejedor and Anderson 1990; Buffeteau et al. 1999; Lee and Sung 2001; Ren and Kato 2002; Buffeteau et al. 2001; Tickanen, Tejedor-Tejedor, and Anderson 1997) have been quantitatively measured from the FTIR/IRS spectra. One advantage of FTIR/IRS over other sampling techniques is that surfactant adsorption at the IRE surface can be studied by in-situ experiments. Generally, the advantage of in-situ investigation of surfactant adsorption is that it offers both the adsorption kinetics and chemical information regarding the adsorption state.

The adsorption density equation was originally derived by Sperline, Muralidharan, and Freiser (1987) and later modified and applied to flotation chemistry research by Miller and co-workers (Jang and Miller 1993; Kellar, Cross, and Miller 1989). The adsorption density equation in one form is

$$\Gamma = 10^{7} \frac{A - NC_b \varepsilon d_e}{N\varepsilon(2d_e/d_p + p/\cos\phi)} \qquad \text{(EQ 2)}$$

where

Γ = adsorption density, μmol/m^2
A = integrated absorbance, cm^{-1}
N = Avogadro's number
C_b = bulk solution concentration, mol/L
ε = absorptivity, L/mol·cm^2
d_e = effective thickness of the sample, cm
d_p = penetration depth, cm
p = number of adsorbate-coated IRE entrance and exit faces

Adsorption density measurements using the FTIR/IRS technique (Figure 19) have shown that at a fluorite surface, monolayer coverage can be achieved at very low initial oleate concentrations (below 1×10^{-6} M). Such behavior is characterized by a monolayer plateau in the adsorption isotherm but is not the case for calcite. For fluorite, chemisorption is clearly the dominant adsorption mechanism at low oleate concentrations with oleate bonding directly with calcium sites at the fluorite surface. Chemisorption also occurs to a more limited extent (incomplete monolayer) at the surface of other calcium minerals, such as calcite and apatite for low oleate concentration. On the other hand, at higher concentrations of oleate and with calcium ion, the growth of multilayers and/or the physical adsorption of calcium dioleate collector colloids are observed from the adsorption isotherm measured using FTIR/IRS spectra.

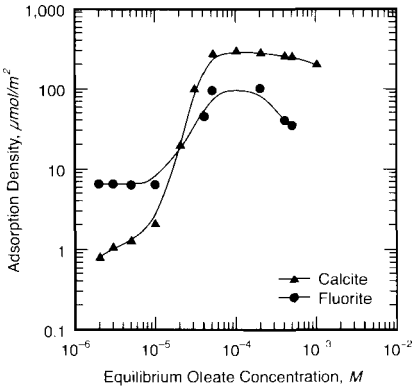

FIGURE 19 Adsorption isotherms of oleate at semisoluble mineral surfaces as determined by direct FTIR/IRS analysis of the surface

Of course, in-situ FTIR/IRS has also been used extensively for qualitative studies of surfactant adsorption at mineral surfaces (Young and Miller 2000; Free and Miller 1996; Lu and Miller 2002). In these studies, high S/N ratios were obtained. These studies have also provided considerable information regarding surfactant adsorption thermodynamics and kinetics. However, it is difficult to obtain information regarding interfacial water structure from in-situ FTIR/IRS experiments (Hancer, Sperline, and Miller 2000).

OTHER VIBRATIONAL SPECTROSCOPY TECHNIQUES

Vibrational spectra, as well as infrared spectroscopy, can be obtained by other spectroscopic techniques such as Raman and sum-frequency generation (SFG). Although it is difficult to obtain detailed information about natural mineral surface composition at monolayer coverage by these experimental techniques, they present other advantages, which are described in the following sections.

Raman Spectroelectrochemistry

Raman spectroscopy is an in-situ technique that is well suited to the investigation of a mineral surface. In Raman spectroscopy, the spectrum of the collected light comprises a series of discrete bands at frequencies higher to (anti-Stokes) or lower than (Stokes) the elastically scattered (Rayleigh) laser line. These lines are said to be Raman shifted from the Rayleigh line, and the shift is equal to vibrational energy of the transition. Minerals may exhibit vibrational spectra because of the structure of the molecular units that they contain as in the case of S–S in pyrite, or the spectra may be derived from the vibrational structure of the mineral crystal (sphalerite) (Hope, Woods, and Munce 2001). Many common materials (e.g., glass and water) are transparent to visible and near-infrared radiation, and they are weak Raman scatterers in the wavelengths where the majority of laser excitation sources operate. The dependence of the Raman shift on the vibrational and rotational transitions of the scattering molecules means that some minerals may not exhibit a significant Raman spectrum, galena and chalcocite being Raman-inactive sulfide minerals.

Raman scattering is an inefficient process with less than 1 in 10^6 photons undergoing a Raman interaction. Typically, this requires a sample thickness of 5 to 50 nm for the spectra

to be detectable with the most sensitive modern commercial instruments. In spectroelectrochemical studies of collector adsorption, electrodes of gold, silver, or copper have been used for surface-enhanced Raman scattering (SERS). This technique enables the formation of a monolayer of adsorbed collector molecules to be characterized. SERS has been used to investigate the adsorption of a range of sulfide mineral flotation collectors: ethyl xanthate (Woods and Hope 1998; Woods, Hope, and Brown 1998a, b); isopropyl, isobutyl, and isoamyl xanthate (Hope, Watling, and Woods 2001b); O-isopropyl-N-ethylthionocarbamate (Woods and Hope 1999); 2-mercaptobenzothiazole (Woods, Hope, and Watling 2000; Hope, Watling, and Woods 2001a); di-isobutyldithiophosphinate (Hope et al. 2003; Hope, Woods and Watling 2003); and butyl ethoxycarbonylthiourea (Hope , Woods and Watling 2001; Hope et al. 2004). In the case of the xanthates, the collector adsorption can be controlled using the electrode potential. Spectra can be obtained from surfaces prior to collector adsorption, with partial monolayer coverage and for multilayet coatings. This behavior can also be observed with thiocarbamates. The Raman spectra of these collectors were consistent with adsorption of the collector molecules on the surface and intact, through a collector sulfur group. Decomposition of a collector was only observed under applied potentials greater than the solution potentials encountered in typical sulfide mineral flotation.

Mercaptobenzothiazole, di-isobutyldithiophosphinate and butyl ethoxycarbonylthiourea flotation reagents adsorbed onto the metallic electrode surface throughout the accessible potential range. The Raman spectra of the deposits formed on the electrode surface were very close to the spectra of the relevant metal compounds prepared in bulk. Metal-collector compounds could be extracted from the electrode surface after extended reaction times and, when characterized by Raman, FTIR, and nuclear magnetic resonance, were found to be the same as the bulk compounds.

Results indicate that sulfide mineral flotation reagents can act either through the chemisorption of collectors (xanthates and thiocarbamates), or through the formation of a metal compound on the mineral surface (mercaptobenzothiazole, di-isobutyldithiophosphinate and butyl ethoxycarbonylthiourea).

Sum-Frequency Generation

SFG was first introduced in 1987 by Shen's research group (Zhu, Suhr, and Shen 1987). Since then, SFG has been further developed into a surface-specific vibrational spectroscopy and used to study the vibrational modes and orientations of molecules and monitor reactions at interfaces. SFG is a nonlinear optical process, where the signal is generated at a frequency that is the sum of the frequencies of two incident optical fields due to the nonlinear interaction of infrared and visible lasers as shown in Figure 20 (Shen 1989). SFG is forbidden in a medium with inversion symmetry, but this nonlinear optical process occurs at surfaces where the inversion symmetry is broken. Most bulk materials have inversion symmetry; thus, they do not generate SFG signals. This unique feature makes SFG a sensitive and powerful tool for the study of various interfaces and surfaces (Nickolov, Wang, and Miller 2004).

The SFG spectrum of molecules with long hydrocarbon chains is very sensitive to hydrocarbon chain order—loosely packed chains and disordered monolayers will, in general, have more random orientations of the methyl and methylene groups, and the intensity of the SFG signal will be much smaller than in the case of an all-trans state. When an alkyl chain is in an all-trans conformation, it is locally centrosymmetric around the C–C bond, and the CH_2 symmetric stretching mode at ~2,850 cm^{-1} is SFG inactive and does not

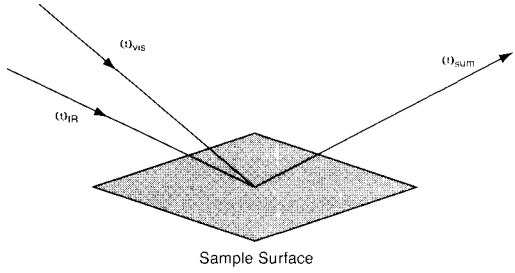

FIGURE 20 SFG generation

appear in the spectra. When the chains are disordered because of gauche defects, this local inversion symmetry is lifted, and a peak at 2,850 cm^{-1} will appear in the spectra to an extent that depends on the degree of disorder. The ratio of intensity of the CH_3 symmetric stretching to CH_2 symmetric stretching can be used to provide a relative measurement of hydrocarbon chain ordering (Conboy et al. 1997). The peak ratio method, which directly depends on intermolecular and intramolecular symmetries, therefore provides the most quantitative measure of chain conformation in the monolayer (Smiley and Richmond 1999). In a closely packed surfactant monolayer in all-trans conformation, there are only two dominant bands at 2,875 cm^{-1} and ~2,940 cm^{-1} that correspond to the symmetric stretching vibration and the symmetric stretching Fermi resonance with a bending overtone of the CH_3 group, respectively.

In the following discussion, the acronyms SSP and SPS (where S and P represent polarization that is perpendicular and parallel, respectively, to the incident plane) designate the state of polarization of the beams in the following order: output sum frequency beam, input visible beam, and input IR signal beam. For example, Figure 21 shows the spectrum for an oleic acid Langmuir–Blodgett (LB) film at the surface of fused silica (Wang 2004). The spectrum suggests that the oleic acid forms a closely packed monolayer in all-trans conformation because there are only two dominant bands at 2,878 cm^{-1} and 2,940 cm^{-1} which correspond to the symmetric stretching vibration and the symmetric stretching Fermi resonance with a bending overtone of the CH_3 group, respectively, in the SSP polarization spectrum. Shown in Figure 22 are the spectra taken from the interface of CaF_2 and a hydroxamic acid D_2O (10^{-3} M hydroxamic acid) solution (Wang 2004). The spectrum for the SSP polarization state is similar to that for a monolayer of hydroxamic acid at a fused silica surface (Wang 2004). The CH_2 symmetric stretching is observed at 2,850 cm^{-1}. The peak at 2,877 cm^{-1} is due to the CH_3 symmetric stretching. The Fermi resonance of CH_3 symmetric stretching appears at 2,940 cm^{-1}. A small peak at 2,920 cm^{-1} is assigned to CH_2 asymmetric stretching. For the SPS polarization state, the major peak is due to CH_3 asymmetric stretching at 2,961 cm^{-1}. The peak from the CH_3 symmetric stretching appearing at 2,880 cm^{-1} for the SPS polarization state indicates that the CH_3 symmetric axis has a certain angle with respect to the surface normal. The SFG intensity from the CH_2 gauche structure is greater than that for the LB-transferred monolayer. The strong CH_3 symmetric stretching peak that appears in the SPS spectrum means there is a significant tilt angle between the C–CH_3 axis and the surface normal.

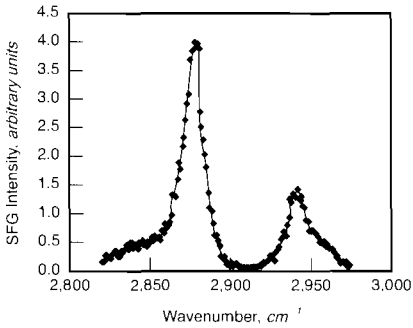

FIGURE 21 SFG spectra for oleic acid LB film at the surface of fused silica under SSP polarization conditions

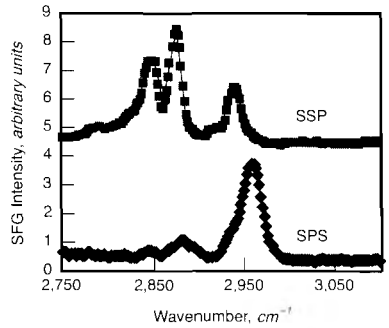

FIGURE 22 SFG spectra taken from hydroxamic acid at D_2O solution/CaF_2 interface SSP and SPS polarization conditions

MICROSCOPY AND MINERALOGY: PAST, PRESENT, AND FUTURE

For many years, traditional descriptive mineralogical examination has been performed using polished sections of samples. Determination of the mineral quantities (modal analysis) and liberation analysis in ores and mineral processing samples has been a basic requirement. The era of quantitative mineralogy (quantitative modal analysis and quantitative liberation analysis) began in 1848 when Delesse published a method to determine the mineral quantities based on the areas of the minerals of interest in a polished section. The method was very labor intensive: it involved tracing the outlines of the mineral grains onto a cloth, sticking this cloth onto a tin foil, cutting the tin foil, sorting according to the different minetals, and then measuring the relative weighting of each group of foil cutouts. The ratio of the weights of the tin foil cutout minerals to the weight of the original tin foil was proportional to the area of that mineral in the sample surface and was correlated to the volume percent and the weight percent.

In 1898, Rosiwal published an improved method to determine the mineral quantities in polished sections. Rosiwal's method, which became known simply as "cord analysis," involved a grid of parallel lines covering the image of the specimen surface that were used to determine the linear length of intercepts onto each mineral of interest. From the addition of the linear intercept in the mineral of interest and the total length of the lines, the linear percent of the mineral was calculated, which was correlated to the volume percent and the weight percent.

In 1934, Glagolev published an imptoved method for determining minerals quantities. Glagolev's method, which became known simply as "point counting," involved manual counting of the points in a grid that coincided with a mineral of interest in a polished section observed with an optical microscope. The ratio of the points on a mineral of interest to all points on the examination grid was equivalent to the volume fraction of that mineral, which was correlated to the weight percent.

The advent of affordable computers in the 1970s allowed the development of systems that improved the speed for detetmining the mineral quantities. Basically, the methods developed by Delesse, Rosival, and Glagolev (area grade, linear grade, and point counting) are behind the computerized systems used to determine the mineral quantities. The advent

of computers also provided the required speed to quantitatively determine the mineral liberation, which basically involves the measurement of the particle mineral composition. A review of the capabilities of early image analysis is given in works by Martens, Morton, and McCarthy (1978) and Taylor et al. (1978). Many of the developments of early image analysis were spurred by the needs of metallography.

In 1974, the CANMET Mining and Mineral Sciences Laboratories (CANMET-MMSL) in Canada adapted a Quantimet system to perform quantitative mineralogy. Petruk (1976) described this system, which was interfaced to an optical reflected light microscope with a black-and-white video camera, and performed measurements of areas of mineral grains. Other systems interfaced to optical microscopes were used in other parts of the world. However, system limitations were soon recognized in that many minerals could not be properly discriminated.

Very early in the development of systems for quantitative mineralogy, it was realized (Jones 1984) that minerals could be better identified automatically by using scanning electron microscopes (SEMs) or electron microprobes (EMPs) with X-ray detectors for elemental analysis. Si(Li) energy-dispersive spectroscopy (EDS) detectors or wavelength-dispersive spectroscopy (WDS) detectors were used.

The system developed by Jones at Imperial College, London, United Kingdom (Jones 1984), was based on an electron microprobe (Camebax) with WDS detectors. The system identified the minerals using linear scans at a pixel size of ~2 μm and the elemental X-ray signals from the WDS detectors. Measurement time was ~10 msec per pixel if the mineral was identified from the presence or absence of an element, and 100 msec if more complete elemental information was required. The identification of a single mineral grain requires acquiring and processing information from 10 to 30 pixel spots.

The QEM*SEM system was developed by the Commonwealth Scientific and Industrial Research Organization (CSIRO) in Australia. It was initially presented by Grant and colleagues in 1976. The present configuration, commercially available, is called QEM*Scan. The system is based on a SEM and identifies minerals mainly based on their elemental X-ray counts obtained from EDS detectors. EDS detectors have a dead time that is a function of the count rate. The first EDS detectors had analog pulse processors and could process a maximum of 25,000 counts per second (cps). Although it was possible to purchase QEM*SEM systems with one EDS detector, to increase its speed the first full configuration of the QEM*SEM had four EDS detectors with analog pulse processing. In the 1990s, EDS detectors with digital pulse processors became available and could process a maximum of ~50,000 cps (the actual count rate of an EDS with analog pulse processors is ~2,000 cps, whereas the actual count rate for an EDS detector with digital pulse processor is ~20,000 cps). The present configuration of the QEM*Scan has four EDS detectors with a digital pulse processor. In general, the system uses a grid of points that are superimposed on the image of the particles. From each of these stop points, the system acquires elemental X-ray information from the group of EDS detectors. The EDS information is compared with a database of minerals, and the mineral at the point is identified. The acquisition time per stop point is fast, ~10 msec. However, because a mineral grain may comprise 10–30 stop points, the overall speed of the system to process several thousands of mineral grains is slow. To partially address speed concerns, the system has different operational modes to perform bulk mineralogical analysis or to perform a more detailed mineralogical analysis including the liberation analysis. In general, the main difference is the spacing of the stop points to acquire EDS X-ray data.

In 1984, a system was integrated at the CANMET-MMSL (Petruk 1988) to determine mineral quantities and liberation analysis by measurements of areas of mineral grains and particles. The system was based on a programmable generic image analyzer interfaced with an electron microprobe (JEOL 733). The highly stable electron beam current in the microprobe allows the system to identify the minerals using mainly the backscattered electron (BSE) image. Acquisition of BSE images is much faster than acquisition of X-ray elemental information. The first generation of the system (1984) was based on an IBAS image analyzer (Kontron) hosted in an MCP computer (Motorola); this system allowed identification and measurement of ~5,000 particles per hour. The last generation of the system is based on a KS400 image analyzer (Zeiss Vision) hosted in a computer that allows identification and measurement of ~100,000 particles per hour. There are ~5,000 known minerals; among those are many minerals with similar average atomic numbers (Z_{av}) and, thus, similar BSE gray levels. However, a given sample does not have 5,000 minerals but probably only ~20 minerals and of those, commonly, only five minerals are of interest. Thus, for many samples, it is possible to use only the information from the BSE image to perform the image analysis. For example, BSE images allow discrimination between pyrrhotite ($Fe_{1-x}S$, $x \sim 0.2$ with Z_{av} = 22.1) and troililite (FeS, with Z_{av} = 22.4), and discrimination between magnetite (Z_{av} = 21.0) and hematite (Zav = 20.1). There are some cases where there are minerals of interest with overlapping BSE gray level. For these cases, the system at CANMET-MMSL can obtain elemental X-ray information from any of its X-ray detectors. The speed of the system is reduced when the image analysis requires the use of X-ray data. The first generation of the system had two WDS detectors and one EDS detector. The image analyzer automatically controls the electron beam and obtains the elemental X-ray information from any of the X-ray detectors. The system can acquire X-ray information from the whole field, or from rectangular windows around the mineral grains or from stop points similar to the QEM*Scan. Thus, the system can identify mineral grains by a combination of BSE imaging and elemental X-ray data. The system could also be operated in a mode fully similar to the QEM*Scan, although it would rarely be necessary (i.e., identifying all minerals based on elemental X-ray information from stop points). In this latter mode, the first generation of image analyzer at CANMET-MMSL was slower than the QEM*Scan, because it used X-ray data from a single X-ray detector (either EDS or WDS).

WDS detectors have better energy resolution than EDS detectors (~5 eV vs. ~140 eV, respectively; e.g., Goldstein et al. 1994). Thus, considering the whole population of ~5,000 existent minerals, there will be minerals whose elements overlap in the EDS spectra but can be well resolved using WDS detectors. However, WDS detectors have focusing limitations (i.e., the signal intensity is not homogeneous for the entire field of view at magnifications lower than ~300×). X-ray information can be acquired very quickly by deflecting the electron beam to a required position at the field of view. This can be done for any magnification using an EDS detector. However, this cannot be done for magnifications lower than ~300× using the WDS detectors, because the count rate for a given mineral will be different at the extreme corners of the field of view. It is possible to automatically control the stage by moving it to a given point to the center of the viewing field and obtaining the X-ray data from a WDS detector. This is known as stage-scanning and is a common feature of modern controllers of electron microprobes. The image analyzer at CANMET-MMSL can be programmed for stage-scanning and using WDS data at low magnifications for minerals that cannot be discriminated by EDS information. However, the speed of the system is further reduced. Another possibility is to acquire BSE images and WDS information at magnifications of

300× or higher and then zoom down the images to a lower magnification that would be better suited to the size of the particles in the sample (Matos, Lastra, and Petruk 1996).

Since 1984, the operational philosophy with the system at CANMET-MMSL has been to discriminate as many minerals of interest as possible using only BSE information and combine the information from EDS or WDS only when needed. Since 1984, having analyzed several thousand samples, the overall experience at CANMET-MMSL has been that ~80% of the sample cases can be analyzed using BSE information only, ~10% can be analyzed by adding single elemental information from the EDS detector, ~5% can be analyzed by adding multiple elemental information from the EDS detector, and another 5% of the sample cases require adding information from the WDS detectors.

There is another advantage of performing quantitative mineralogy based on BSE imaging. This is related to the excitation volume than can be demonstrated from first physical principles. X-ray signals from electron-based instruments do not come from an area on the sample surface; rather, they come from an excitation volume. This excitation volume is a function of the accelerating voltage of the electron beam and the density of the sample point. In general terms, the diameter of the excitation volume for X-ray signals from minerals is ~3 μm at 20 kV of accelerating voltage. On the other hand, the BSE signal provides a spatial resolution of ~0.1–0.2 μm. Thus, for grains smaller than ~3–5 μm, the X-ray signals will give information that may not be appropriate to properly identify the corresponding mineral. Similarly, because the spatial resolution of X-ray signals is ~3 μm for minerals, borders of mineral particles and borders of minerals within particles may not be properly identified.

In the late 1990s, QEM*SEM became QEM*Scan based on a LEO (Zeiss) SEM. At about the same time, Kontron imaging was acquired by Zeiss, whereby Kontron interfaces for SEM instruments and electron microprobes became unavailable, and the Julius Kruttschnitt Mineral Research Centre (JKMRC, Australia) developed the Mineral Liberation Analyser (MLA) (Gu 2003). The MLA is based on a SEM (FEI, formerly Philips), and is commercially available. The MLA is similar to the system at CANMET-MMSL. The MLA discriminates many minerals of interest using only BSE information and combines with information from EDS only when needed to discriminate certain specific minerals. When analyzing only BSE images, the system is faster than the QEM*Scan. The MLA has up to two EDS detectors; therefore, when identifying minerals based solely on X-ray information, it is slower than the QEM*Scan.

In 1997, a new type of X-ray energy-dispersive detector for SEM instruments and electron microprobes was introduced. This new technology is based on the silicon drift chamber (SDC) detector (Figure 23). The SDC detector does not require cooling by liquid nitrogen, and its count rate capability is extremely high at ~400,000 to 1,000,000 cps. Thus, one SDC detector at a count rate of 400,000 is equivalent to ~8 conventional EDS detectors with digital pulse processor (Figure 24). Initially, the SDC detectors had a beryllium window and could not detect elements lighter than ~Na. In addition, the energy resolution was not as good as that obtained by conventional EDS detectors. Thus, the electron microscopy community was not very enthusiastic in adopting SDC detectors. Presently, SDC detectors are available with a polymer window and can detect elements lighter than Na. In addition, by compromising on the count rate, SDC detectors can achieve better energy resolution than conventional EDS detectors. It is also possible to obtain counts from a combination of four SDC detectors to acquire even higher count rates.

The present configuration of the image analyzer at CANMET-MMSL is still based on an electron microprobe with two WDS detectors and one EDS detector, but it has an

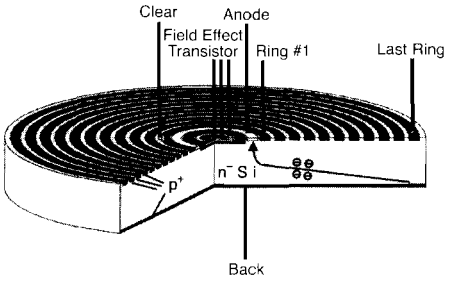

FIGURE 23 General scheme of the SDC detector

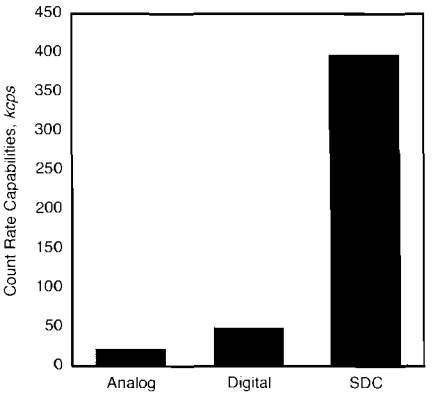

FIGURE 24 Differences in count rate capabilities of different EDS detectors at similar energy resolutions (analog = conventional EDS detector with analog pulse processor; digital = conventional EDS detector with digital pulse processor; SDC = silicon drift chamber detector)

additional SDC detector (Röntec). The SDC detector allows acquisition times of 10 msec per pixel and shorter times if electron beam currents of at least 15 nA are used. In full BSE mode, the system at CANMET-MMSL processes ~100,000 particles per hour. In full X-ray mode, it processes ~20,000 particles per hour; it is presently faster than any commercially available systems. Speed is important, especially when considering the analysis of tailing samples that contain very few grains of the mineral of interest, a common situation when investigating the losses of valuable minerals.

Electron microprobes are instruments that are designed to provide very stable electron beam currents. A stable electron beam current is a basic requirement for EMP analysis. The electron beam current in an EMP is stable over a period of weeks and can be automatically monitored and maintained constant every second. On the other hand, the SEM is basically an imaging instrument and typically provides less-stable electron beam currents. In many SEM instruments, the electron beam current varies over periods of 1 hour (Gu 2003). To fully exploit the speed of quantitative mineralogy based on BSE imaging, the instrument must provide a stable electron beam current over the full time of sample analysis. To analyze a set of samples or to search and analyze precious minerals, the electron beam current must be stable during a period of up to 24 hours. In addition, the EMP can yield higher beam currents than the SEM. Higher beam currents yield better contrast between minerals in the BSE image. Also, EMP instruments commonly have four large ports and two additional auxiliary ports. These six ports can be used to connect a range of X-ray detectors. Thus, EMP instruments are better suited for quantitative mineralogy studies.

Without budget constrictions, the future instruments for quantitative mineralogy studies will be EMPs with two WDS detectors, each with four analyzing crystals and four SDC detectors. The cost of these instruments could be similar to the cost of the present commercially available systems for quantitative mineralogy studies. Of course, there will be some simpler instruments for basic requirements and limited budgets.

X-RAY ABSORPTION SPECTROSCOPY

Practically, X-ray absorption spectroscopy (XAS) must be carried out on a synchrotron radiation source to provide the wide X-ray wavelength range and high intensity required. XAS is primarily of use in mineral flotation studies where information about the form of trace elements is required; that is, the form of the element that is of interest is not obscured by the signal from the same element within the bulk sample. However, in certain modes, XAS can also be used to probe surface phenomena where the element of interest is also present in the underlying specimen. Surprisingly, XAS has been used relatively rarely for mineral flotation studies, although there are a number of advantages to its use as compared to techniques that require a vacuum environment. There is generally little sample preparation required, and the sample turnaround time is rapid as most measurements can be carried out in air. XAS measurements lend themselves to the use of environmental cells and provide both spatial and electronic structure information.

XAS can be divided into several subtechniques, which are more commonly referred to in the literature (for a general review of XAS and other synchrotron techniques, see Gerson, Halfpenny et al. 1999). In general, XAS is divided into two categories: XANES (X-ray absorption near-edge structure), and EXAFS (extended X-ray absorption fine structure). The former occurs up to approximately 40 eV above the absorption edge and is the result of excitation from the valence to conduction bands. XANES is sensitive to the coordination geometry and oxidation state. EXAFS results from scattering of excited photoelectrons off neighboring atoms and occurs at higher incident energies than XANES. EXAFS is sensitive to local structure out to approximately 5 Å.

XAS can be measured in several modes. Most commonly, the X-ray fluorescence (measured at 90° to the incident X-ray beam) or transmitted intensities are measured. Transmission measurements enable the bulk sample to be probed, whereas fluorescence measurements are more surface sensitive with a measurement depth dependent on the energy of the fluorescence yield (see, e.g., Kasrai et al. 1996). However, both measurement modes can be used effectively to study surface-related phenomena where the element under investigation is surface specific.

More surface-sensitive measurements can be obtained using total electron yield (TEY), partial electron yield (PEY) or reflection EXAFS (REFLEXAFS). TEY is measured via the drain current experienced on electron excitation to the continuum. The depth of analysis of this form of XAS is dependent on the incident X-ray energy. Thus, for the Si L-edge (95–120 eV) the depth of measurement is about 50 Å, whereas for the Si K-edge this would be approximately 700 Å (1,830–1,900 eV) (Kasrai et al. 1996). PEY is obtained via the measurement of electron current induced on a conducting grid a short distance from the sample surface. A voltage can be applied to the grid to repel low-energy electrons (i.e., those resulting from deeper within the sample). REFLEXAFS requires the incident beam to intercept the surface at a very low angle, thus enabling reflection rather than absorption. An angle of 100 millidegrees, half of the critical angle for chalcopyrite, has been adopted (England et al. 1999b). In this instance, the depth of penetration was less than 50 Å. The data can be collected via measurement of the intensity of the reflected beam or the fluorescence yield at 90° to the sample surface. This enables surface-sensitive measurements to be obtained at monolayer or even sub-monolayer coverage (Greaves 1991). However, REFLEXAFS requires a flat, polished specimen, whereas the other modes of measurement can be carried out on powders, slurries, or liquids.

XAS has been used for the study of Zn and Pb sorption onto chalcopyrite ($CuFeS_2$) (England et al. 1999a, b and references therein). Chalcopyrite tends to have natural hydrophobicity and thus self-floatability. This characteristic is attributable to the formation of a sulfur-rich surface layer due to metal loss under conditions of low pH. The adsorption of metal cations, as hydroxides, can result in a reduction in the flotation response. REFLEXAFS data revealed that Zn adsorbed at pH 5.5 is bonded to O (at 2.00 Å) only. There was no evidence of bonding to S. On addition of xanthate (at pH 10.2), the Zn coordination changed radically so that the nearest neighbor coordination sphere contained both O and S (at 1.97 Å and 2.33 Å, respectively). For Pb adsorption, both O and S coordination is present prior to the addition of xanthate. After xanthate addition, only S coordination is observed. It appears, therefore, that the initial adsorption site of the Zn species is onto the oxidized $Fe(OH)_x$ species present on the surface, whereas the Pb is adsorbed onto the sulfur-rich surface regions. This interpretation provides an explanation for the observation that only small amounts of Pb in solution are required to remove chalcopyrite self-flotation. Adsorption of Pb (probably as a hydroxide) would render the hydrophobic sulfur-rich regions hydrophilic. The loss of self-floatability would be much less affected by adsorption of Zn species onto the already hydrophilic, oxidized Fe surface regions.

Another study, originating from the same research team, examined the adsorption of Cu and Pb onto sphalerite (ZnS) (England et al. 1999a; Pattrick et al. 1998, 1999). Cu adsorption activates the sphalerite surface for enhanced collector adsorption. ZnSe was also examined, as an isostructural analogue to sphalerite so that the sulfur XAS data could be obtained from the adsorbed xanthate without the spectra being swamped by bulk S contributions. On the basis of analysis of the REFLEXAFS data, it was proposed that 3 S atoms and 1 O atom are bonded to the adsorbed Cu atoms (at 2.25 Å and 2.07 Å, respectively). On addition of xanthate, the O were replaced by an S atom. The fourth S atom has a considerably longer bond distance to the Cu atom as compared to the three initial S atoms, 2.75 Å as compared to 2.22 Å. Pb adsorbed onto sphalerite was proposed to be coordinated solely to O atoms. On addition of xanthate, the Pb coordination consisted of two bonds to S and two to O. It would appear, therefore, that, at least under the conditions used for this study, Pb does not specifically adsorb onto sphalerite as does Cu.

A similar study of the adsorption of Cu onto sphalerite has also been carried out by Gerson, Lange et al. (1999). Analysis of the EXAFS data indicated Cu coordination to S (2.26–2.30 Å) but no evidence of Cu coordination to O. A data set plus Fourier transform for Cu adsorbed onto sphalerite sample are shown in Figures 25a and 25b. The Fourier transform is similar to a one-dimensional electron density distribution surrounding but offset by a phase shift. The large central amplitude is the result of the surrounding S atoms. The other two maxima centered at approximately 1 Å and 2.7 Å are the result of the truncation of the Fourier transform series from the experimental data. The exact location of the maxima will depend on the data range that is fitted by the simulated model data. In order to fit, the analytical program must truncate the model data in a manner similar to the experimental data. It is unclear in the studies by Pattrick et al. (1999) whether the interpretation of O coordination is, in fact, the result of this artefact induced by Fourier series truncation.

On the basis of the interpretation of the EXAFS and XANES data, together with other experimental evidence and previous knowledge, a mechanism for the Cu activation of sphalerite was presented by Gerson, Lange et al. (1999). This mechanism proposes the replacement of Zn by Cu on the sphalerite surface to form a distorted trigonal planar structure, similar to the Cu structure found for half the Cu atoms within covellite (CuS). In-situ

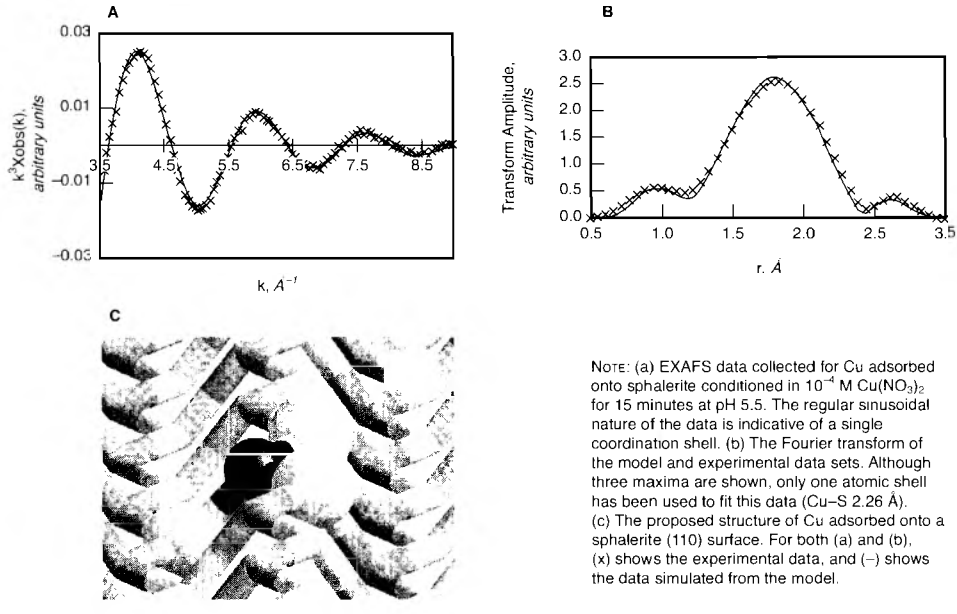

NOTE: (a) EXAFS data collected for Cu adsorbed onto sphalerite conditioned in 10^{-4} M $Cu(NO_3)_2$ for 15 minutes at pH 5.5. The regular sinusoidal nature of the data is indicative of a single coordination shell. (b) The Fourier transform of the model and experimental data sets. Although three maxima are shown, only one atomic shell has been used to fit this data (Cu–S 2.26 Å). (c) The proposed structure of Cu adsorbed onto a sphalerite (110) surface. For both (a) and (b), (x) shows the experimental data, and (–) shows the data simulated from the model.

FIGURE 25 Experimental EXAFS data sets with correspondence to proposed copper structure

reduction of Cu(II) to Cu(I) occurs, resulting in the oxidation of the surrounding S atoms. This smearing out of the surface charge results in the increased degree of hydrophobicity for Cu-activated sphalerite as compared to unactivated sphalerite that has been observed and, hence, results in increased floatability even without collector addition. The conditions under which Cu activations were carried out during this study were carefully chosen to inhibit copper(II) hydroxide ($Cu(OH)_2$) formation.

The Cu activation of pyrite (FeS_2) has also been investigated by Weisener and Gerson (2000). On the basis of EXAFS data, a similar structure for adsorbed Cu to that projected for sphalerite was proposed (i.e., distorted trigonal planar) and near-identical Cu–S bond lengths were determined. Again, there was no evidence of Cu–O coordination except in the instance where $Cu(OH)_2$ was purposefully precipitated within the activating solution (pH 8.5, 2.84×10^{-4} mol m^{-2} Cu). In this instance, Cu–S bond lengths of 2.29 Å and Cu–O bond lengths of 2.00 Å were derived from the EXAFS data. This also provides a possible explanation for the observations by Pattrick et al. (1999) as to the coordination of adsorbed Cu to O.

Todd and Sherman (2003) used XAS to probe the surface oxidation mechanism of chalcocite (Cu_2S). This leads to reduced flotation of chalcocite in minerals processing circuits. In this instance, TEY collection mode was used. For the Cu L-edge measurements undertaken, there is likely to be a contribution from the bulk mineral. However, the O K-edge measurements will be surface specific only because of the absence of O in the bulk. Oxidation of chalcocite in different pH solutions indicated that under acidic pH, cuprous oxide (Cu_2O) dominates the oxidation products, whereas under alkaline pH, cupric oxide (CuO) is the major oxidation product.

XANES has been employed in a study of selected elements (Ti, V, Cr, Mn, and As) in deep-cleaned Kentucky No. 9 coal (Huggins et al. 1997). Tail and float samples were prepared

using both a Denver cell and column flotation. The tails and float fractions were examined in order to gain a better understanding of the distribution and form of elements that may be released during combustion and therefore form a pollutant risk and, hence, to identify appropriate coal-cleaning strategies. XANES data has been interpreted through comparison with data obtained from standards. V, Ti, Cr, and Mn were all found to be different in form in the tail and float fractions. The tailings fraction was interpreted as containing Ti and V in interlayer positions within illite, whereas the Ti and V present in the float fraction was proposed to be in an organic association. The pre-edge features from the V spectra indicate the oxidation state of V to be higher in the float fraction than in the tails fractions. The difference between the data collected for Cr in the float and tailings fraction was found to be subtler with Cr present in the tails as illite and in float fractions as a hydroxide species. Mn in the tails was associated with calcite ($CaCO_3$) and illite, whereas in the float fraction, two different organic forms were identified. The XANES data for the float fractions for these elements suggest the principal coordination is to O anions. In contrast, As was primarily associated with pyrite and oxidation products thereof, and the relative proportions of these forms was not float or tail dependent.

Additional opportunities exist to further utilize XAS measurements to advance the understanding of mineral flotation studies. In particular, an opportunity exists to exploit energy-dispersive XAS for mineral processing applications. This type of measurement can be carried out rapidly as it uses a broadband incident X-ray beam rather than the monochromatic beam traditionally employed. The latter requires a monochromator sweep in order to scan the energy range required for the spectra. Energy-dispersive XAS can be carried out on in-situ materials and in real time. Data acquisition can be carried out in the order of 10 seconds.

SCANNED PROBE MICROSCOPIES

Though the scanned probe microscopies—scanning tunneling microscopy (STM), and atomic force microscopy (AFM)—are essentially research tools applied to model systems, they have added much in the last two decades to the understanding of surface reactions and adsorption mechanisms of minerals under flotation-related conditions. Both techniques can image surfaces close to the atomic level. STM requires reasonably conductive samples (which has made galena a mineral of choice) with some chemical identification in scanning tunneling spectroscopic mode. AFM can image insulating surfaces, cannot chemically identify atoms, but can give astonishing information on particle–particle and even particle–bubble interactions and changes with reaction and adsorption in force–distance (approach–retract) mode. Hochella (1995) has reviewed STM and AFM studies of mineral surfaces and their oxidation. Smart, Amarantidis et al. (2003) have reviewed applications to oxidation and collector additions in flotation. Some examples of particular insights, related to surface processes described previously, will illustrate the unique types of information that these techniques can provide.

The development of isolated, patchwise oxidation in air and solution has been very well illustrated by STM studies of galena surfaces. Eggleston and Hochella (1990, 1991, 1992) have imaged (001) surfaces of galena at atomic scale after exposure to water for 1 minute. Apparent vacancies at the sulfur sites are correlated with oxidation in their model of this process. The oxidized regions do not initiate randomly, but after oxidation has begun at a site, these regions tend to nucleate and grow without initiation of new sites. The boundaries of the oxidized regions tend to lie along the [110] directions, apparently due to S atoms

across this front having only one nearest-neighbor-oxidized sulfur whereas an unoxidized S across a [100] boundary would have two nearest-neighbor-oxidized sulfurs. As with crystallization processes, [100] fronts move fast and disappear, leaving the slow-moving [110] dominant.

At lower magnification, the process of galena oxidation in air has also demonstrated random sites of oxidation and growth on (001) galena surfaces with no clear preference for initiation at step edges or corners (Laajalehto et al. 1993). This process is illustrated in Figure 26 from that work and correlated with XPS spectra, showing that the initial oxidation products are peroxide, hydroxide, and carbonate species successively. With time up to 270 minutes in air, the oxidation products grow from surface features with lateral dimensions <0.6 nm to overlapped regions >9 nm diameter with "holes" in the overlayer that still allow access to the underlying sulfide surface. Further studies of galena oxidation in air (Kim et al. 1994), comparing synthetic and natural galena samples, confirmed that the growth mechanism on natural galena with the oxidation initiation sites correlated with impurity atoms in the surface layer. The very much slower oxidation of synthetic galena did occur preferentially on edges, dislocations, and lattice defect sites on the (001) faces of the galena crystal. The XPS spectra in this case show predominantly lead hydroxide and sulfate with a smaller contribution from carbonate in the oxidation products.

In solution, STM (and AFM) imaging showed the development of subnanometer pits with increasing reaction time in air-purged water at pH 7 (Kim et al. 1995). The boundaries of the pits lie in the (100) and (010) directions in the galena surface with depths corresponding to unit cell dimensions of galena (i.e., 0.3 and 0.6 nm). The process occurring in solution is congruent dissolution, confirmed by XPS spectra showing unaltered Pb4f and S 2p signals. The x- and y-dimensions of the pits and their rates of formation depend strongly on the pH and purging gas (i.e., O_2, air, N_2) used. Dissolution rates, determined directly from STM images of monolayers removed, decrease with increasing pH in agreement with the reported dissolution studies on galena (Fornasiero, Ralston, and Smart 1994;

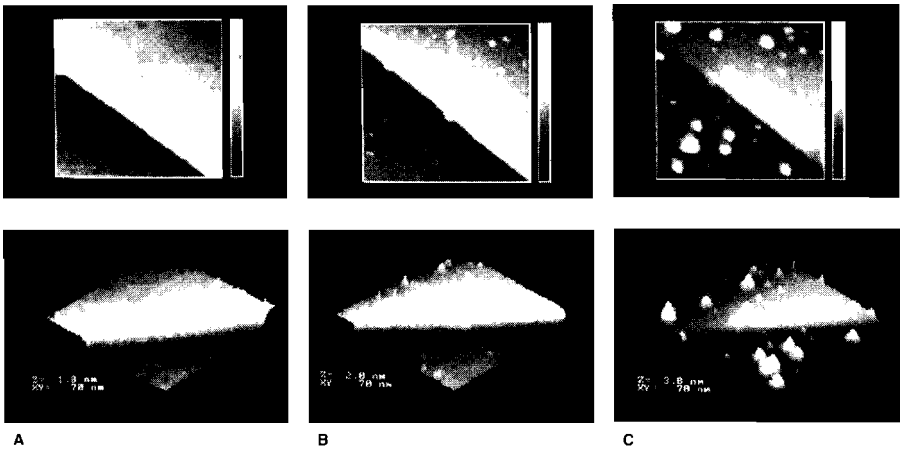

FIGURE 26 STM images from a 70 x 70 nm area of (a) freshly cleaned galena surface; (b) the same surface after 70 minutes standing in air; (c) after 270 minutes in air. The upper row are grayscale images; the lower row are 3-D (rotated) images with the vertical scales 1.8, 2.0, and 3.8 nm, respectively. Constant current mode (0.2–0.25 nA), bias ~0.35 V.

Hsieh and Huang 1989). For all pH values studied, the growth of the dissolution pits is significantly greater in the x- and y-directions than in the z-direction, suggesting that the edges are more active toward dissolution than the faces (Kim et al. 1995). At the relatively low surface-area-to volume ratios used in the STM studies, there is no evidence for the growth of surface oxidation products similar to those observed in air or to adsorption/precipitation of lead hydroxide colloids from solution. Increasing the lead ion concentration to 10^{-3} M in solution resulted in surface product formation as elongated, oval colloidal projections with dimensions of ~50 nm × 20 nm and average heights of 14 nm, with a distinct [110] directionality. XPS analysis has confirmed that these species are predominantly lead hydroxide, presumably formed from the hydrolysis of lead ions followed by surface attachment. It is not yet clear whether the mechanism of surface attachment involves the formation of lead hydroxide colloids in solution and their precipitation onto the galena surface or adsorption of $Pb^{2+}/Pb(OH)_2$ molecular species at specific sites on the galena surface before in-situ growth. However, the formation of these patchy surface layers shows that the galena surface is heterogeneous and that its overall hydrophobicity and flotation response will be controlled not only by the surface chemistry but by the surface arrangement of hydrophilic and hydrophobic patches. Atomic level imaging of the (001) surface of galena, reviewed by Hochella (1995), has been achieved, including observation of the oxidation of a single S site at which the tunneling current has been effectively extinguished.

In-situ STM images of a freshly cleaved galena crystal in contact with an air-equilibrated 10^{-4} M ethyl xanthate solution show colloidal particles of lead ethyl xanthate (as confirmed by XPS and FTIR) formed at the surface corresponding to multilayer surface coverage. In-situ STM studies of ethyl xanthate treated preoxidized galena surfaces have also shown the removal of oxidized lead species and the formation of colloidal lead ethyl xanthate particles as flattened spheres with diameters of 10–20 nm and average heights of 6 nm (Ralston 1994b; Kim et al. 1995).

Combined XPS and AFM studies of galena oxidation in acetate buffer (pH 4.9) by Wittstock et al. (1996) produced dramatic imaging of elemental sulfur protrusions 10–200 nm after initial roughening of the galena surface. These protrusions are separated by several hundred nanometers and appear to result from a process of diffusion in the aqueous phase. XPS shows the formation of elemental sulfur starting at potentials more anodic than 160 mV SHE (saturated hydrogen electrode). AFM imaging first detects the protrusions at +236 mV SHE. The authors, therefore, propose that the process causing surface roughening is dissolution of PbS to Pb(II) ions and HS^- ions, whereas the deposition reaction is the electrochemical oxidation of HS^- ions to elemental sulfur. It seems likely that sulfur formation starts at impurity locations leading to different rates and sizes of protrusion development.

In nickel sulfide processing, magnesium silicate (MgO) gangue minerals often report to the concentrate, causing downstream processing problems as well as increased smelting costs. In addition, these hydrophilic MgO minerals may interfere with the flotation of valuable sulfide minerals such as pentlandite [$(Fe, Ni)_9S_8$]. Flotation of the MgO particles may be via composite particles or through attachment to the valuable minerals as slime coatings. A coating of hydrophilic slime particles will decrease the hydrophobicity of the sulfide particle and may also reduce collector adsorption (Learmont and Iwasaki 1984). Either of these flotation mechanisms will reduce both the flotation rate and recovery, and will, therefore, result in lower recoveries of the valuable sulfide minerals (Trahar 1981; Senior and Trahar 1991; Wellham, Elber, and Yan 1992). Slime coatings of lizardite and chrysotile have been found to adhere to the surface of pentlandite, reducing its flotation rate (Edwards, Kipkie,

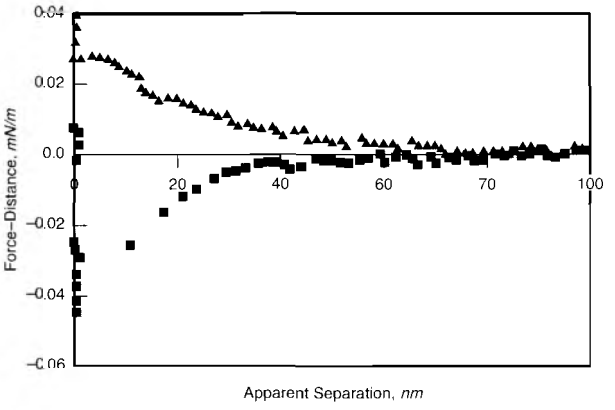

FIGURE 27 Direct interaction forces as a function of apparent separation measured on approach between a pentlandite surface (■) and lizardite particle (▲) in 10^{-3} M KNO_3 (potassium nitrate) at pH 9.4 and in the presence of 20 ppm CMC

and Agar 1980; Li 1993; Chen at al. 1999a, b; McQuie 1999). The interaction between lizardite and pentlandite has been directly investigated using the atomic force microscope in force–distance mode and electrokinetic zeta potential determinations as a function of pH and in the presence of the polymeric dispersant, carboxymethyl cellulose (CMC) (Bremmell, Fornasiero, and Ralston 2005). The lizardite mineral was positively charged with the zeta potential independent of pH. The magnitude and sign of the pentlandite particles were pH dependent and were negative for pH values above 4.5. At pH values greater than 9, where flotation of nickel sulfide ores is routinely performed, the two minerals are oppositely charged and, therefore, attract through an electrostatic mechanism. Direct interaction force measurements between pentlandite and lizardite surfaces as a function of pH demonstrate this attractive interaction. Adsorption of CMC at the lizardite–solution interface overcompensates the positive charge on the lizardite particle, and its zeta potential is rendered negative. In the presence of CMC, a repulsive interaction force between lizardite and pentlandite, which was concluded to be of electrosteric origin, was measured in the AFM (Figure 27). The results explain the flotation behavior of the minerals performed in this and previous studies.

PLANT CASE STUDY: USING SURFACE ANALYSIS TO EXAMINE ZINC CIRCUIT MINERAL LOSSES

Introduction

The Matagami mine sulfide flotation plant in Northern Quebec is the focus operation for this study. The Matagami plant produces copper and zinc concentrates. This study investigated zinc losses in the zinc circuit using surface analysis. For this work, the rougher feed, rougher concentrate, rougher tails, cleaner tails, and zinc concentrate streams were sampled and examined in the CANMET-MMSL surface science laboratories located in Ottawa, Canada. Pulp samples were collected using established and modified protocols designed to preserve the surface chemistry on particles from the time of sampling until the time of analysis. The surface chemistry of particles in each pulp was examined using the surface analysis methods of X-ray photoelectron spectroscopy (XPS) and Auger electron spectroscopy

(AES). The bulk mineralogy of each pulp sample was determined from X-ray diffraction (XRD) powder patterns. XRD was used because the materials are crystalline, and the method has a detection range that is readily comparable to that of XPS. Standard XPS provides excellent chemical state information, but the spatial resolution of the data is limited to hundreds of micrometers. For the acquisition of surface chemical information from individual particles, AES was used. The spatial resolution of the AES surface chemical data collected using a scanning Auger microprobe is limited essentially by the diameter of the primary electron beam; therefore, AES spectra can be collected from exceedingly small particles.

Methods

To prevent the exposure of individual particle surfaces to air and preserve the chemistry of the solid–liquid interface present at the time of collection, the sampling steps outlined in the next section were followed. These procedures are in a continual state of development and are the product of discussion, consultation, and experimentation with surface science groups in academia, government, and industry in Africa, Australia, Europe, and North America. The protocols are based on the premise that each particle in a pulp will have a hydrated boundary layer that will prevent direct contact between the particle surface and the atmosphere. When frozen, it is a passivating and protecting layer of ice that isolates individual particles from the air (Smart 1991; Love, Cayless, and Hazell 1993; Pratt, Nesbitt, and Muir 1994).

Pulp samples were prepared for XRD analysis by grinding 2 g of material to less than 10-μm particle diameters using a custom micromill. XRD analyses were conducted on the samples using an automated Rigaku diffractometer equipped with a rotating copper anode X-ray source. XRD powder patterns were collected using monochromatic radiation; they were then processed, and the mineral phases were identified using the Materials Data Inc. powder diffraction pattern analysis program JADE (Release 6.1) and the ICDD Powder Diffraction Database (Release 2001).

XPS spectra were collected using a PerkinElmer Corporation (Physical Electronics Division) PHI-5600 spectrometer equipped with an OMNI V lens system. XPS data were collected using 400-W achromatic Mg X-rays ($E_{x\text{-}ray}$ = 1,353.6 eV) and Al X-rays ($E_{x\text{-}ray}$ = 1,486.6 eV). The two X-ray sources were utilized as a means of resolving contributions from coincident photoelectron and X-ray-induced Auger electron emissions. The energy scale of the spectrometer was calibrated to the metallic Au($4f_{7/2}$) line at 84.0 eV and was to give an energy dispersion of 857.8 eV between the metallic copper $2p_{3/2}$ and 3p lines. The analyzer pass energy was 187.0 eV for broad-energy-range "survey" scans and 29.35 eV for narrow-energy-range "multiplex" scans. The binding energy scale of the spectra is referenced to the C1s peak from adventitious hydrocarbon (static charge referencing) fixed at 285.0 eV (Swift 1982). XPS information was collected from spots measuring nearly 400 μm in diameter, and the vacuum in the analytical chamber was approximately 8.0×10^{-10} Torr during analysis. Details on the analysis of XPS spectra are provided in work by Pratt, Nesbitt, and Muir (1994).

AES spectra were collected using a PerkinElmer Corporation (Physical Electronics Division) PHI-600 scanning Auger microprobe equipped with a LaB_6 thermionic electron emitter. Analyses were obtained using an electron beam accelerated to a potential of 3.0 kV at a current of 90 nA and an analyzer energy resolution set to 0.6%. Under these instrument conditions, exceedingly small particles could be examined without any interferences from the sample mount matrix. This is because the volume of analysis is defined by the primary

beam diameter (~300 nm) and the escape depth (λ) of Auger electrons, which is approximately 1 to 3 nm beneath a particle surface. Lambda (λ) is dependent on the kinetic energy of the Auger electron and the solid's density. Semiquantitative surface compositions were calculated using peak-to-peak heights and manufacturer-supplied, empirically-derived sensitivity factors. The vacuum in the analytical chamber was about 6.0×10^{-10} Torr during analysis.

Metallurgical Processing Surface Science Protocols for Sampling and Analysis

The experimental protocol for preparation of surface samples is as follows:

1. Sample the pulp stream using a beaker.
2. Place several milliliters of pulp into a vial.
3. Purge with $N_2(g)$.
4. Cap the vial and seal the cap with silicon.
5. Freeze the sample as quickly as possible, and maintain in a frozen state until time for analysis.
6. Thaw the sample within 30 minutes of the scheduled analysis.
7. Using a pipette, remove 1.5 mL of the process water and deposit it into a micro test tube.
8. Using a micro spatula, remove a minute amount of pulp and place it into the micro test tube. For XPS-destined samples, the solution should be slightly clouded; this amount provides about a monolayer of particle coverage on the filter. For AES-destined samples, the solution should remain clear; this amount provides the dispersed particle coverage needed for Auger analysis.
9. Separate the solids from the solution onto a 2.5-cm-diameter 0.45-μm nitrocellulose membrane filter using a vacuum filtration system. (NOTE: For these experiments, the membrane filter was sputter-coated with gold to increase conductivity and fixed to the appropriate sample platen.)
10. Prepare the damp samples for surface analysis using an ultrahigh vacuum (UHV) conditioning chamber that is attached to the XPS instrument. (NOTE: The conditioning chamber used in these experiments was designed and built by one of the authors. One function of the conditioning chamber is to prepare damp samples for the UHV conditions required for spectroscopic surface analysis. The chamber design is attached to the XPS via a series of UHV gate valves and stainless-steel conduits to the analytical chamber of the XPS. This permits all manipulations to be undertaken at high to ultrahigh vacuum conditions. Conditioning takes up to 15 hours; therefore, UHV conditions should be maintained throughout the experiment.)
11. For collection of AES data, transfer the conditioned samples to the scanning Auger microscope instrument from the XPS using a high-vacuum transfer vessel. (NOTE: The high-vacuum transfer vessel used in these experiments was designed and built at CANMET by Dr. Jim Brown.)

Results and Discussion

The XRD powder pattern and XPS survey scan data collected from the selected zinc circuit feeds and the concentrates show that there is a progressive lessening in complexity with the evolution of the pulps within the circuit. This discussion focuses on the results obtained from the sphalerite component in the pulps. Contributions from sphalerite can be identified

in XRD patterns collected from each of the pulps examined. XPS survey scans collected from each of the pulps show contributions that can be attributed to sphalerite as well. They also show distinct Cu contributions. Qualitative evaluation of the XRD data shows that only minor to trace amounts of chalcopyrite ($CuFeS_2$) can be found in the pulps. The source for the Cu detected by XPS is most likely the Cu added for activation of sphalerite. Because the vast majority of the particles in the Zn concentrate is sphalerite, the approximate surface Zn/Cu ratio of 3:1, obtained from this pulp, can be used as a model ratio for the qualitative evaluation of sphalerite activation in each of the pulps examined. The approximate Zn/Cu ratios for the pulps examined are as follows: rougher feed >30:1, rougher concentrate 4:1, rougher tails 10:1, and cleaner scavenger tails 6:1.

As inadvertent activation of the sphalerite in the feed should not be very high, a high Zn/Cu ratio is expected. Activation appears to have occurred within the rougher, and the rougher concentrate has the appropriate Cu activation ratio. For the rougher tails, the high Zn/Cu ratio obtained may indicate that the small amount of sphalerite present in the pulp has not been sufficiently activated. For the cleaner scavenger tails, the Zn/Cu ratio is about 50% greater than the model ratio. These results indicate that there is a problem with the activation of the sphalerite in the circuit.

Information into Cu chemistry at particle surfaces can be obtained through evaluation of Cu 2p spectra collected from the rougher concentrate, rougher tails, cleaner scavenger tails, and Zn concentrate (Figure 28). The spectra have been normalized such that the intensities near 932 eV are nearly coincident. The overlain spectra are characterized by Cu $2p_{3/2}$ and $2p_{1/2}$ peaks, respectively, at 931.8 eV and 951.7 eV. The mineralogy of the Zn concentrate is mainly sphalerite, and the Cu 2p collected from this pulp is interpreted to originate from activated sphalerite surfaces. The shapes and positions of the Cu 2p peaks are similar to those reported for Cu(I) (Chawala, Sankarraman, and Payer 1992), and, in agreement, the signals are interpreted to originate from Cu(I) ions. The pulp with activated surfaces most closely resembling those of the Zn concentrate data is the rougher concentrate data. The Cu 2p spectra collected from the rougher tails and cleaner scavenger tails have an additional contribution near 942 eV. The position and shape resemble those reported for Cu(II) ions (Chawala, Sankarraman, and Payer 1992) and are interpreted to be from Cu(II) species. These results show that a portion of the Cu on the sphalerite surfaces in the tails is found as Cu(II).

AES Analyses of Individual Sphalerite Particles

AES spectra were collected from individual sphalerite particles in the process stream pulps. A minimum of 10 particles in each pulp was analyzed. The AES spectra showed contributions from S, C, O, and the transition metals Fe, Cu, and Zn. On many of the sphalerite particles examined, contributions from Ca were detected. Two spectra representative of the AES data collected in the study are shown in Figure 29.

The Ca detected is interpreted to be associated with a precipitated Ca sulfate species, possibly gypsum. Although the sampling size is small, the AES results show that Ca concentrations are consistently the lowest on sphalerite particles in concentrates. Conversely, Ca concentrations are consistently higher on sphalerite particles in tails.

Using O concentrations as a guide to the degree of surface oxidation, the AES data shows that the tails have sphalerite particles that are the more oxidized (Figure 29a), and the two concentrate pulps have sphalerite particles that are the least oxidized (Figure 29b). These trends appear to apply to both the coarse and fine particles examined within the pulps.

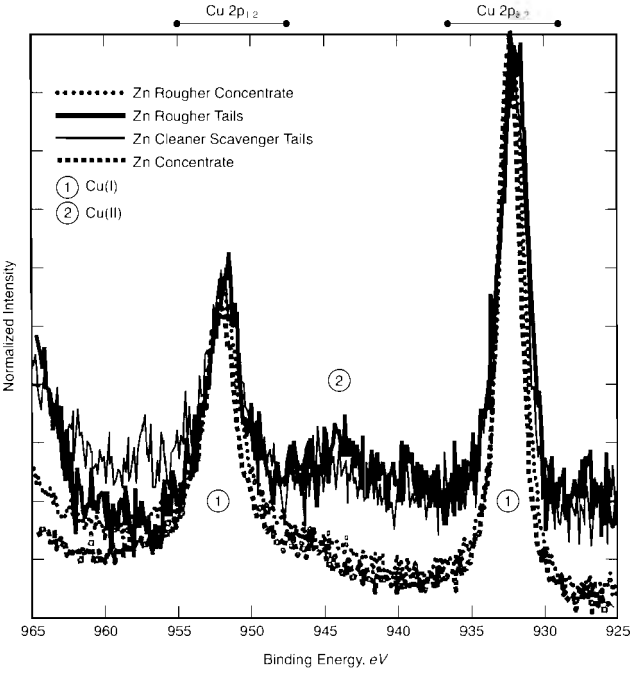

FIGURE 28 Overlain narrow region Cu 2p spectra collected from four zinc circuit pulps. The peak intensities shown have been normalized. The dotted traces are the concentrates and the solid traces are the tails.

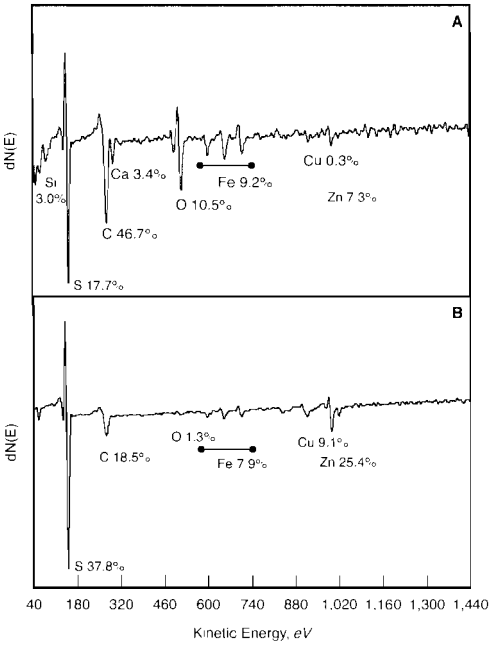

FIGURE 29 Representative AES scans collected from sphalerite particles in the (a) cleaner scavenger tails and (b) zinc concentrate. Values are atomic %.

XRD shows that an appreciable amount of sphalerite is found in tailings pulps within the circuit, and the XPS results show that the sphalerite is found in the tails because of inadequate Cu activation. Examination of the Auger spectra collected from individual sphalerite particles in the circuit pulps corroborates the XPS interpretation. The sphalerite particles examined in the two concentrate pulps show well-defined Cu peaks (Figure 29b). Those in the tails have no clear and unambiguous contributions from Cu (Figure 29a). The number of particles examined is small and a larger sample population would greatly increase the confidence in the interpretations put forward for the Auger data.

SUMMARY

AES examination of sphalerite in the two concentrates shows that these particles are less oxidized and cleaner (less calcium species) than those in the two tails. The XPS and AES results show that sphalerite component in the tails has not been sufficiently activated, and the XPS results show oxidized copper is found on the surface of the particles.

REFERENCES

Ahlberg, E., K.S.E. Forssberg, and X. Wang. 1990. The surface oxidation of pyrite in alkaline solution. *J. Appl. Electrochem.* 20:1033–1039.

Bolin, N.J., S.L. Chryssoulis, and C.J. Martin. 1997. A surface study of Boliden ore by TOF-LIMS. *Int. J. Miner. Process.* 51:27–37.

Bremmell, K.E., D. Fornasiero, and J. Ralston. 2005. Pentlandite-lizardite interactions and implications for their separation by flotation. *Colloids Surfaces A* 252:207–212.

Briggs, D., and M.C. Seah, editors. 1992. *Practical Surface Analysis.* 2nd edition. Volume 1: Auger and X-ray Photoelectron Spectroscopy. United Kingdom: John Wiley & Sons.

Brinen, J.S., S. Greenhouse, D.R. Nagaraj, and J. Lee. 1993. SIMS and SIMS imaging studies of adsorbed dialkyl dithiophosphinates on PbS crystal surfaces. *Int. J. Miner. Process.* 38:93–109.

Bronold, M., Y. Tomm, and W. Jaegermann. 1994. Surface states of cubic d-band semiconductor pyrite FeS_2. *Surf. Sci.* 314:L931–L936.

Buckley, A.N., I.C. Hamilton, and R. Woods. 1985. Investigation of the surface oxidation of sulfide minerals by linear potential sweep voltammetry and X-ray photoelectron spectroscopy. Pages 41–60 in *Flotation of Sulfide Minerals.* Edited by K.S.E. Forssberg. Amsterdam: Elsevier.

Buckley, A.N., and R. Woods. 1987. The surface oxidation of pyrite. *Appl. Surf. Sci.* 27:347–452.

———. 1991. Adsorption of ethyl xanthate on freshly exposed galena surfaces. *Colloids Surf.* 53:33–45.

Buffeteau, T., D. Blaudez, E. Pere, and B.B. Desbat. 1999. Optical constant determination in the infrared of uniaxially oriented monolayers from transmittance and reflectance measurements. *J. Phys. Chem. B* 103:5020.

Buffeteau, T., E. Le Calvez, B. Desbat, I. Pelletier, and M. Pezolet. 2001. Quantitative orientation of α-helical polypeptides by attenuated total reflection infrared spectroscopy. *J. Phys. Chem. B* 105:1464.

Carlson, T.A. 1975. *Photoelectron and Auger Spectroscopy.* New York: Plenum Press.

Chawala, S.K., N. Sankarraman, and J.H. Payer. 1992. Diagnostic spectra for XPS analysis of Cu-O-S-H compounds. *J. Electron Spectrosc.* 61:1–18.

Chen, G., S. Grano, S. Sobieraj, and J. Ralston. 1999a. The effect of high intensity conditioning on the flotation of a nickel ore. Part 1: Size-by-size analysis. *Miner. Eng.* 12:1185–1200.

———. 1999b. The effect of high intensity conditioning on the flotation of a nickel ore. Part 2: Mechanisms. *Miner. Eng.* 12:1359–1373.

Chryssoulis, S.L. 2001. Using mineralogy to optimize gold recovery by flotation. *JOM* 53:48–50.

Chryssoulis, S.L., L.J. Cabri, J.L. Campbell, and W.J. Teesdale. 1991. Comparison of in-situ gold analyses in arsenian pyrite. *Appl. Geochem.* 6:225–230.

Chryssoulis, S.L., R. Dunne, and A. Coetzee. 2004. Diagnostic microbeam technology in gold ore processing. *JOM* 56(7):53–57.

Chryssoulis, S.L, J.Y. Kim, and K.G. Stowe. 1994. LIMS study of variables affecting sphalerite flotation. Proceedings of the 26th Annual Meeting of the Canadian Mineral Processors. Paper no. 28. Office of the Secretary of the Canadian Mineral Processors.

Chryssoulis, S.L., F. Reich, and K.G. Stowe. 1992. Characterization of mineral surface composition by laser probe microanalysis. *Trans. Inst. Min. Metall., Sect. C* 100:1–6.

Chryssoulis, S.L., K.G. Stowe, E. Niehuis, H.G. Cramer, C. Bendel, and J.Y. Kim. 1995. Detection of collectors on concentrator mineral grains by time of flight secondary ion mass spectrometry TOF-SIMS. *Trans. Inst. Min. Metall., Sect. C* 104:141–150.

Chryssoulis, S.L., C.G. Weisener, and S. Dimov. 1995. Detection of mineral collectors by TOF-LIMS. Pages 899–902 in *Proceedings of the Secondary Ion Mass Spectrometry SIMS X*. Edited by A. Benninghoven, B. Hagenhoff, and H.W. Werner. New York: John Wiley & Sons.

Clarke, N.S., J.C. Ruckman, and A.R. Davey. 1986. Laser microprobe mass spectrometry of solid surfaces. In *Proceedings of the Third International Laser Microprobe Mass Spectrometry Workshop*. Edited by F. Adams and L. van Vaeck. Belgium: University of Antwerp.

Conboy, J.C., M.C. Messmer, R. Walker, and G.L. Richmond. 1997. An investigation of surfactant behavior at the liquid/liquid interface with sum frequency vibrational spectroscopy. Amphiphiles at Interfaces. *Prog. Colloid Polym. Sci.* 103:10.

Delesse, A. 1848. Procédé mechanique pour determiner la composition des roches. 4th series. *Annales des Mines* 13:379–388.

Dimov, S., and S.L. Chryssoulis. 1997. Relative sensitivity factors for quantitative TOF-LIMS analysis of mineral surfaces. Pages 815–818 in *Proceedings of the 11th International Conference on Secondary Ion Mass Spectrometry–SIMS XI*. Edited by G. Gillen, R. Lareau, J. Bennett, and F. Stevie. New York: John Wiley & Sons.

Edwards, G.R., W.B. Kipkie, and G.E. Agar. 1980. The effect of slime coatings of the serpentine minerals, chrysotile and lizardite on pentlandite flotation. *Int. J. Miner. Process.* 7:33–24.

Eggleston, C.M., and M.F. Hochella Jr. 1990. Scanning tunneling microscopy of sulfide surfaces. *Geochim. Cosmochim. Acta* 54:1511–1517.

———. 1991. Scanning tunneling microscopy of galena 100 surface oxidation and sorption of aqueous gold. *Science* 254:983–986.

———. 1992. Tunneling spectroscopy applied to PbS001 surfaces: Fresh surfaces, oxidation and sorption of aqueous Au. *Am. Mineral.* 78:877–883.

England, K.E.R., R.A.D. Pattrick, J.M. Charnock, and J.F.W. Mosselmans. 1999a. Floating sulfide: Activating and poisoning surfaces. *J. Synchrotron Rad.* 6:664–666.

———. 1999b. Zinc and lead sorption on the surface of $CuFeS_2$: A fluorescence REFLEXAFS study. *Int. J. Miner. Process.* 57:59–71.

Fa, K., and J.D. Miller. 2003. Surfactant adsorption density calculation from Fourier transform infrared external reflection spectroscopy FTIR/ERS. *J. Chem. Phys.* 119(24):13068.

Finkelstein, N.P. 1997. The activation of sulfide minerals for flotation: A review. *Int. J. Miner. Process.* 52:81–120.

Fornasiero, D., F. Li, J. Ralston, and R.St.C. Smart. 1994. Oxidation of galena surfaces, I. X-ray photoelectron spectroscopic and dissolution kinetics studies. *J. Colloid Interface Sci.* 164:333–344.

Free, M.L., and J.D. Miller. 1996. The significance of collector colloid adsorption phenomena in the fluorite/oleate flotation system as revealed by FTIR/IRS and solution chemistry analysis. *Int. J. Miner. Process.* 48:197.

Frew, J.A. K.J. Davey, R.M. Glen, and R.St.C. Smart. 1994. Effects of fine grinding on flotation performance: Zinc regrind at Cominco Alaska's Red Dog mine. Pages 287–288 in *Proceedings of the 5th Mill Operators' Conference*. Melbourne: Australasian Institute of Mining and Metallurgy.

Frew, J.A., R.St.C. Smart, and E.V. Manlapig. 1994. Effects of fine grinding on flotation performance: Generic statements. Pages 245–250 in *Proceedings of the 5th Mill Operators' Conference*. Melbourne: Australasian Institute of Mining and Metallurgy.

Gerson, A.R., P.J. Halfpenny, S. Pizzini, R. Ristić, K.H. Roberts, D.B. Sheen, and J.N. Sherwood. 1999. Applications of synchrotron X-radiation to problems in materials science. Pages 105–169 in *X-ray Characterization of Materials*. Edited by E. Lifshin. New York: Wiley-VCH.

Gerson, A.R., A.G. Lange, K.P. Prince, and R.St.C. Smart. 1999. The mechanism of copper activation of sphalerite. *Appl. Surface Sci.* 137:207–223.

Glagolev, A.A. 1934. Quantitative analysis with the microscope with the microscope by the point method. *Eng. Min. J.* 135:399–400.

Goh, S.W., A.N. Buckley, R.N. Lamb, R.A. Rosenberg and D. Moran. 2006. The oxidation states of copper and iron in mineral sulfides, and the oxides formed on initial exposure of chalcopyrite and bornite to air. *Geochim. et Cosmochim. Acta* 70(9):2210–2228.

Goh, S.W., A.N. Buckley, R.N. Lamb, W.M. Skinner, A. Pring, H. Wang, L-J. Fan, L-Y. Jang, L-J. Lai and Y-W. Yang. 2006. Sulfur electronic environments in a-NiS and b-NiS: Examination of the relationship between coordination number and core electron binding energies. *Phys. Chem. Minerals* 33:98–105.

Goldstein, J.I., D.A. Newbury, P. Echlin, D.C. Joy, A.D. Romig, C.E. Lyman, C. Fiori, and E. Lifshin. 1994. Comparison of WDS and EDS. Pages 331–336 in *Scanning Electron Microscopy and X-ray Microanalysis*. 2nd edition. New York: Plenum Press.

Grano, S., J. Ralston, and R.St.C. Smart. 1990. Influence of electrochemical environment on the flotation behavior of Mt. Isa copper and lead-zinc ore. *Int. J. Miner. Process.* 30:69–97.

Grano, S.R., D.W. Lauder, N.W. Johnson, S. Sobieraj, R.St.C. Smart, and J. Ralston. 1993. Surface analysis as a tool for problem solving: A case study of the Hilton concentrator at Mt. Isa Mines Ltd. Pages 1–15 in *Proceedings of the Symposium Polymetallic Sulfides Iberian Pyrite Belt (Evora, Portugal)*. Lisbon: Portuguese Mining Industry Association.

Grano, S.R., P.L. Wong, W. Skinner, N.W. Johnson, and J. Ralston. 1996. Detection and control of calcium sulfate precipitation in the Hilton concentrator of Mt. Isa Mines, Ltd. Pages 171–179 in *Proceedings of the XIX International Journal of Mineral Processing Congress*, Australia. Volume 3. Melbourne: Australasian Institute of Mining and Metallurgy.

Grant, G., J.S. Hall, A.F. Reaid, and M.A. Zuiderwyk. 1976. Multi-compositional particle characterization using a SEM microprobe. Pages 401–408 in *Scanning Electron Microscopy*. Volume III. Chicago: ITT Research Institute.

Greaves, G.N. 1991. Glancing angle X-ray absorption spectroscopy. *Adv. X-ray Anal.* 34:13–22.

Gu, Y. 2003. Automated scanning electron microscope based mineral liberation analysis. *J Miner. Mater. Charact. Eng.* 2(1):33–41.

Hancer, M., R.P. Sperline, and J.D. Miller. 2000. Anomalous dispersion effects in the IR-ATR spectroscopy of water. *Appl. Spectrosc.* 18(1):138.

Harmer, S.L., and H.W. Nesbitt. 2004. Stabilization of pyrite FeS_2, marcasite FeS_2, arsenopyrite FeAsS and loellingite $FeAs_2$ surfaces by polymerization and auto-redox reactions. *Surf. Sci.* 564:38–52.

Harmer, S.L., A.R. Pratt, H.W. Nesbitt, and M.E. Fleet. 2004. Sulfur species at chalcopyrite $CuFeS_2$ fracture surfaces. *Am. Mineral.* 89:1026–1032.

Hart, B., M. Biesinger, J.D. Miller, J. Francis, and R.St.C. Smart. 2004. Principal component analysis applied to surface chemistry in minerals flotation. Pages 73–88 in *Particle Size Enlargement in Mineral Processing, Proceedings of the Fifth UBC McGill International Conference on Fundamentals of Mineral Processing*. Edited by J.S. Laskowski. Montreal: Canadian Institute of Mining, Metallurgy and Petroleum.

Hart, B., M.C. Biesinger, and R.St.C. Smart. 2006. Improved statistical methods applied to surface chemistry in minerals flotation. *Miner. Eng.* 19:790–798.

Hochella, M.F., Jr. 1995. Mineral surfaces: Their characterisation and their chemical, physical and reactive natures. Pages 17–60 in *Mineral Surfaces*. Edited by D.J. Vaughan and R.A.D. Pattrick. London: Chapman and Hall.

Hope, G.A., K. Watling, and R. Woods. 2001a. An electrochemical investigation of the suppression of silver dissolution in aqueous cyanide by 2 mercaptobenzothiazole. *J. Appl. Electrochem.* 31:703–709.

———. 2001b. A SERS spectroelectrochemical investigation of the interaction of isopropyl, isobutyl and isoamyl xanthates with silver. *Colloids Surf. A* 178:157–166.

Hope, G.A., R. Woods, S. Boyd, and K. Watling. 2003. A spectroelectrochemical investigation of the interaction of diisobutyldithiophosphinate with copper, silver and gold surfaces: I. Raman and NMR spectra of diisobutyldithiophosphinate compounds. *Colloids Surf.* 214:77–85.

———. 2004. A SERS spectroelectrochemical investigation of the interaction of butylethoxycarbonylthiourea with copper surfaces. *Colloids Surf. A* 232:129–137.

Hope, G.A., R. Woods, and C.G. Munce. 2001. Raman microprobe mineral identification. *Miner. Eng.* 14:1565–1577.

Hope, G.A., R. Woods, and K. Watling. 2001. A spectroelectrochemical investigation of the influence of sodium diisobutyldithiophosphinate on silver dissolution in aqueous cyanide. *J. Appl. Electrochem.* 31:1285–1291.

———. 2003. A spectroelectrochemical investigation of the interaction of diisobutyldithiophosphinate with copper, silver and gold surfaces: II. Electrochemistry and Raman spectroscopy. *Colloids Surf.* 214:87–97.

Hsieh, Y.H., and C.P. Huang. 1989. The dissolution of PbS in dilute aqueous solutions. *J. Colloid Interface Sci.* 131:537–549.

Huggins, F.E., S. Srikantapura, B.K. Parekh, L. Blanchard, and J.D. Robinson. 1997. XANES spectroscopic characterization of deep-cleaned fraction of Kentucky No. 9 coal. *Energy Fuels* 11:691–701.

Jang, W.H., and J.D. Miller. 1993. Verification of the internal reflection spectroscopy adsorption density equation by Fourier transform infrared spectroscopy analysis of transferred Langmuir-Blodgett films. *Langmuir* 9:3159.

———. 1995. Molecular orientation of Langmuir-Blodgett and self-assembled monolayers of stearate species at a fluorite surface as described by linear dichroism theory. *J. Phys. Chem.* 99:10272.

Jones, M.P. 1984. Recent advances in the rapid collection of quantitative mineralogical data. Pages 141–155 in *Applied Mineralogy ICAM 84.* Edited by W.C. Park, D.M. Hansen, and R.D. Hagni. New York: American Institute of Mining, Metallurgical, and Petroleum Engineers.

Kartio, I.J., K. Laajalehto, E. Suoninen, A.N. Buckley, and R. Woods. 1998. The initial products of the anodic oxidation of galena in acidic solution and the influence of mineral stoichiometry. *Colloids Surf. A* 133:303–311.

Kasrai, M., W.N. Lennard, R.W. Brunner, G.M. Bancroft, J.A. Badwell, and K.H. Tan. 1996. Sampling depth of total electron and fluorescence measurements in Si L- and K-edge absorption spectroscopy. *Appl. Surf. Sci.* 99:303–312.

Kellar, J.J., W.M. Cross, and J.D. Miller. 1989. Adsorption density calculations from in situ FT-IR/IRS data at dilute surfactant concentrations. *Appl. Spectrosc.* 43(8):1456.

Kim, B.S., R.A. Hayes, C.A. Prestidge, J. Ralston, and R.St.C. Smart. 1994. Scanning tunneling microscopy studies of galena: The mechanism of oxidation in air. *Appl. Surf. Sci.* 78:385–397.

———. 1995. Scanning tunneling microscopy studies of galena: The mechanisms of oxidation in aqueous solution. *Langmuir* 11:2554–2562.

Kim, J.Y., S.L. Chryssoulis, and K.G. Stowe. 1995. Effects of lead ions in sulphide flotation. Paper 9 in *Proceedings of the 27th Annual Meeting of the Canadian Mineral Processors.* Office of the Secretary of the Canadian Mineral Processors.

Kim, J.Y., J.E. Nesset, S. Parker, and S.L. Chryssoulis. 1997. TOF-LIMS studies of pH modifiers in sulphide flotation. Pages 807–810 in *Proceedings of the 11th International Conference on Secondary Ion Mass Spectrometry, SIMS XI.* Edited by G. Gillen, R. Lareau, J. Bennett, and F. Stevie. New York: John Wiley & Sons.

Kristall, Z., S.R. Grano, K. Reynolds, R.St.C. Smart, and J. Ralston. 1994. An investigation of sphalerite flotation in the Murchison Zinc concentrator. Pages 171–180 in *Proceedings of the 5th Mill Operators' Conference.* Melbourne: Australasian Institute of Mining and Metallurgy.

Laajalehto, K., I. Kartio, T.L. Karila, T.L. Laiho, and E. Suoninen. 1996. Investigation of copper sulfide mineral surfaces using synchrotron radiation excited photoemission spectroscopy. Pages 717–720 in *Proceedings of the European Conference on Applications of Surface and Interface Analysis ECASIA '95.* Edited by H.J. Mathieu, N. Reihl, and D. Briggs. New York: Wiley.

Laajalehto, K., R.St.C. Smart, J. Ralston, and E. Suoninen. 1993. STM and XPS investigation of reaction of galena in air. *Appl. Surf. Sci.* 64:29–39.

Lange, A.G., W.M. Skinner, and R.St.C. Smart. 1997. Fine:coarse particle interactions and aggregation in sphalerite flotation. *Miner. Eng.* 10(7):681–693.

Lascelles, D., and J.A. Finch. 2002. Quantifying accidental activation 1. Cu ion production. *Miner. Eng.* 15:567–571.

Learmont, M.E., and I. Iwasaki. 1984. Effect of grinding media on galena flotation. *Miner. Metall. Process.* 1:136–143.

Lee, S., and C.S.P. Sung. 2001. Surface chemical composition analysis in polystyrene/poly(vinyl methyl ether) blend films by UV reflection spectroscopy. *Macromolecules* 34:599.

Leiro, J.A., K. Laajalehto, I. Kartio, and M.H. Heinonen. 1998. Surface core-level shift and phonon broadening in PbS 100. *Surf. Sci.* 412–413:L918–L923.

Leppinen, J., and J.A. Mielczarski. 1986. Spectroscopic study of the adsorption of thiol collectors on lead sulphide in the presence of sodium sulphide. *Int. J. Miner. Process.* 18:3–20.

Li, Z. 1993. Effect of gangue minerals containing magnesium on pentlandite flotation. *Kuangye Xueyuan Xuebao* 24:36–44.

Love, C.J., R.A. Cayless, and L.B. Hazell. 1993. The SPLINT technique for sample preservation using liquid nitrogen transfer. *Surf. Interface Anal.* 20:565–568.

Lu, Y., and J.D. Miller. 2002. Carboxyl stretching vibrations of spontaneously adsorbed and LB-transferred calcium carboxylates as determined by FTIR internal reflection spectroscopy. *J. Colloid Interface Sci.* 256:41.

Martens, A.E., R.R.A. Morton, and J.C. McCarthy. 1978. The application of advanced image analysis techniques. Pages 426–432 in *Proceedings of the Symposium on Quantitative Analysis of Microstructures in Materials Science, Biology and Medicine*. Edited by J.L. Chermant. Stuggart, Germany: Rieder-Verlag GmbH.

Matos, M.J., R. Lastra, and W. Petruk. 1996. Characterization of feldspar texture and liberation by automated image analysis. *Trans. Inst. Min. Metall., Sect. C* 105:133–140.

McCarron, J.J., G.W. Walker, and A.N. Buckley. 1990. An X-ray photoelectron spectroscopic investigation of chalcopyrite and pyrite surfaces after conditioning in sodium sulfide solutions. *Int. J. Miner. Process.* 30:1–16.

McQuie, J.D. 1999. Influence of particle aggregation and pulp chemistry on the flotation of pentlandite fines in the slimes stream at Mt. Keith. MappSc thesis, University of South Australia, Adelaide.

Mielczarski, E., Y. Duval, and J.A. Mielczarski. 2002. Spectroscopic characterization of the nature and structure of adsorbed organic monolayers on quartz in the region of very strong absorption of substrate. Reverse surface selection rule. *J. Phys. Chem. B* 106(46):11985–11992.

Mielczarski, E., and J.A. Mielczarski. 2003a. Influence of galvanic effect on adsorption of xanthate on pyrite, galena and chalcopyrite. Pages 866–873 in *Proceedings of the XXII International Mineral Processing Congress*, Cape Town, South Africa, September 29–October 3. Volume 2. Edited by L. Lorenzen, et al. Johannesburg: South African Institute of Mining and Metallurgy.

———. 2003b. Surface modification at molecular level in mineral beneficiation. *Int. J. Min. Proc.* 72(1–4):129–140.

———. 2005. Infrared spectroscopic studies of galvanic effect influence on surface modification of sulfide minerals by surfactant adsorption. *Environ. Sci. Technol.* 39:6117–6122.

Mielczarski, E., J.A. Mielczarski, and J.M. Cases. 1998. Molecular recognition effect in monolayer formation of oleate on fluorite. *Langmuir* 14:1739–47.

Mielczarski, E., J.A. Mielczarski, J.M. Cases, B. Rai, and Pradip. 2002. Influence of solution conditions and mineral surface structure on the formation of oleate adsorption layers on fluorite. *Colloids Surf.* 205:73–84

Mielczarski, E., J.A. Mielczarski, Z. Lei, and P. Somasundaran. 2004. Structure of adsorbed n-dodecyl-β-D-maltoside layers on hematite. *J. Colloid Interface Sci.* 275:403–409.

Mielczarski, J.A. 1986. In situ ATR IR spectroscopic study of xanthate adsorption on marcasite. *Colloids Surf.* 17:251–271.

———. 1993. External reflection infrared spectroscopy at metallic, semiconductor and nonmetallic substrates. I. Monolayers films. *J. Phys. Chem.* 97:2649–2663.

Mielczarski, J.A., J. Cases, E. Mielczarski, P. Marion, M. Fordham, and C. Valente. 1999. Production of clean copper sulphide concentrate. In *Proceedings of the Rewas'99 Global Symposium on Recycling Waste Treatment and Clean Technologies*, San Sebastian, Spain, September 5–9. Warrendale, PA: The Minerals, Metals and Materials Society.

Mielczarski, J.A., and E. Mielczarski. 1995. Determination of molecular orientation and thickness of self-assembled monolayers of oleate on apatite by FTIR reflection spectroscopy. *J. Phys. Chem.* 99:3206–3217.

———. 1999. Infrared external reflection spectroscopy of adsorbed monolayers in a region of strong absorption of substrate. *J. Phys. Chem.* 103:5852–5859.

Mielczarski, J.A., E. Mielczarski, and J.M. Cases. 1996. Interaction of amyl xanthate with chalcopyrite, tetrahedrite and tennantite at controlled potentials. Simulation and spectroelectrochemical results for two component adsorption layers. *Langmuir* 12:6521–6529.

———. 1997. Infrared evaluation of composition and structure of ethyl xanthate monolayers produced on chalcopyrite, tetrahedrite and tennantite at controlled potentials. *J. Colloid. Interface Sci.* 188:150–161.

———. 1998. Influence of chain length on adsorption of xanthates on chalcopyrite. *Int. J. Miner. Process.* 52:215–231.

———. 1999. Dynamic of fluorite-oleate interactions. *Langmuir* 15:500–508.

Mielczarski, J.A., E. Mielczarski, J. Zachwieja, and J.M. Cases. 1995. In situ and ex situ infrared studies of nature and structure of thiol monolayers adsorbed on cuprous sulfide at controlled potential. *Langmuir* 11:2787–2799.

Mielczarski, J.A., P. Nowak, and J.W. Strojek. 1980. Spectrophotometric investigation on products of ethyl xanthate sorption on lead sulphide and galena surfaces. Part I. Oxidized samples. *Pol. J. Chem.* 54:279–91.

———. 1983. Correlation between the adsorption of sodium dodecyl sulphate on calcium fluorine fluorite and its floatability—an infrared internal reflection spectroscopy study. *Int. J. Miner. Process.* 11:303–317.

Mielczarski, J.A., Z. Xu, and J.M. Cases. 1996. Qualitative and quantitative evaluation of heterogeneous adsorbed monolayers on mineral electrodes by infrared reflection spectroscopy. *J. Phys. Chem.* 100:7181–7184.

Mielczarski, J.A., and R.-H. Yoon. 1989. FTIR external reflection study of molecular orientation in spontaneously adsorbed layers on low absorption substrates. *J. Phys. Chem.* 93:2034–2038.

Mycroft, J.R., G.M. Bancroft, N.S. McIntyre, J.W. Lorimer, and I.R. Hill. 1990. Detection of sulfur and polysulfide on electrochemically oxidized pyrite surfaces by XPS and Raman spectroscopy. *J. Electroanal. Chem.* 292:139–152.

Nesbitt, H.W., G.M. Bancroft, A.R. Pratt, and M.J. Scaini. 1998. Sulfur and iron surface states on fractured pyrite surfaces. *Am. Mineral.* 83:1067–1076.

Nesbitt, H.W., A.G. Schaufuss, G.M. Bancroft, and R. Szargan. 2002. Crystal orbital contributions to the pyrrhotite valence band with XPS evidence for weak Fe-Fe p bond formation. *Phys. Chem. Miner.* 29(1):72–77.

Nesbitt, H.W., A.G. Schaufuss, M. Scaini, G.M. Bancroft, and R. Szargan. 2001. XPS measurement of fivefold and sixfold co-ordinated sulfur in pyrrhotites and evidence for millerite and pyrrhotite surface species. *Am. Mineral.* 86:318–326.

Nesbitt, H.W., A.G. Schaufuss, M.J. Scaini, H. Hochst, G.M. Bancroft, and R. Szargan. 2003. Monitoring fundamental reactions at NiAsS surfaces by synchrotron radiation X-ray photoelectron spectroscopy: As and S air oxidation by consecutive reaction schemes. *Geochim. Cosmochim. Acta* 67:845–858.

Nesbitt, H.W., I. Uhlig, G.M. Bancroft, and R. Szargan. 2003. Resonant XPS study of the pyrite valence band with implications for molecular orbital contributions. *Am. Mineral.* 88:1279–1286.

Nesbitt, H.W., I. Uhlig, and R. Szargan. 2002. Surface reconstruction and As-polymerization at fractured loellingite $FeAs_2$ surfaces. *Am. Mineral.* 87:1000–1004.

Nesset, J.E., C. Sui, J.Y. Kim, M. Cooper, M. Li, and S.L. Chryssoulis. 2001. The effect of soda ash and lime as pH modifiers in sphalerite flotation. Annual Meeting of the Canadian Mineral Processors. Office of the Secretary of the Canadian Mineral Processors.

Nickolov, Z.S., X. Wang, and J.D. Miller. 2004. Liquid-air interfacial structure of alcohol-octyl hydroxamic acid mixtures: A study by sum-frequency spectroscopy. *Spectrochim. Acta A* 60A(12):2711.

O'Connor, D.J., B.A. Sexton, and R.St.C. Smart, editors. 2003. *Surface Analysis Methods in Materials Science*. 2nd edition. Springer Series in Surface Science. Berlin: Springer-Verlag.

Pattrick, R.A.D., J.M. Charnock, K.E.R. England, J.F.W. Mosselmans, and K. Wright. 1998. Lead sorption on the surface of ZnS with relevance to flotation: A fluorescence REFLEXAFS study. *Miner. Eng.* 11:1025–1033.

Pattrick, R.A.D., K.E.R. England, J.M. Charnock, and J.F.W. Mosselmans. 1999. Copper activation of sphalerite and its relation to flotation: An X-ray absorption spectroscopy reflection extended X-ray absorption fine structure investigation. *Int. J. Miner. Process.* 55:247–265.

Paulucci, G., and K.C. Prince. 1990. Surface core-level shift of lead sulfide. *Phys. Rev. B* 41:3851–3853.

Petruk, W. 1976. The application of quantitative mineralogical analyses of ores to ore dressing. *CIM Bull.* 69(767):146–153.

———. 1988. Capabilities of the microprobe Kontron image analysis system: Application to mineral beneficiation. *Scanning Microsc.* 2(3):1247–1256.

Piantadosi, C. 2001. Competitive collector adsorption in the selective flotation of galena and chalcopyrite from iron sulphide minerals. Ph.D. thesis, University of South Australia, Adelaide.

Piantadosi, C., M. Jasieniak, W.M. Skinner, and R.St.C. Smart. 2000. Statistical comparison of surface species in flotation concentrates and tails from ToF-SIMS evidence. *Miner. Eng.* 13:1377–1394.

Piantadosi, C., B.L. Pyke, and R.St.C. Smart. 2001. TOF-SIMS statistical analysis of surface hydrophobic-hydrophilic species ratios and contact angle estimation in real ore systems. Pages 305–323 in *Interactions in Mineral Processing*. Edited by J.A. Finch, S.R. Rao, and L. Huang. Toronto: Metallurgical Society.

Piantadosi, C., and R.St.C. Smart. 2002. Statistical comparison of hydrophobic and hydrophilic species on galena and pyrite particles in flotation concentrates and tails from TOF-SIMS evidence. *Int. J. Miner. Process.* 64:43–54.

Pratt, A.R., H.W. Nesbitt, and I.J. Muir. 1994. Generation of acids in mine waste: Oxidative leaching of pyrrhotite in dilute H_2SO_4 solutions pH 3.0. *Geochim. Cosmochim. Acta* 58:5147–5159.

Prestidge, C.A., and J. Ralston. 1995. Contact angle studies of galena particles. *J. Colloid Interface Sci.* 172:302–310.

Prestidge, C.A., A.G. Thiel, J. Ralston, and R.St.C. Smart. 1994. The interaction of ethyl xanthate with copper II-activated zinc sulfide: Kinetic effects. *Colloid Surf. A* 85:51–68.

Ralston, J. 1994a. Bubble-particle capture. Page 1464 in *Flotation II*. Volume 2. Edited by S. Castro and J. Alvarez. Chile: Andros.

———. 1994b. The chemistry of galena flotation: Principles and practice. *Miner. Eng.* 7:715–735.

Ren, Y., and T. Kato. 2002. Polarized infrared external reflection spectroscopy of a uniaxial monolayer at the air-water interface. *Langmuir* 18:6699.

Rosiwal, A. 1898. Über Geometrische Gesteinsanalysen. Ein einfacher Weg zür ziffermassigen Feststellung des Quantitätsverhältnisses der Mineral-Bestandteilc gemengter Gesteine, Verh, Kaiserlich Koeniglichen Geologischen Reichsanstaet, Vienna, 5/6. (Translated by H.C. Ranson. On Geometric Rock Analysis. Pages 143–75 in *A Simple Method for the Numerical Determination of the Quantitative Ratios of the Mineral Fractions of Mixed Rocks*. Farnborough, UK: Royal Aircraft Establ. Lib. Trans. No. 871, 1960.)

Ruckman, J.C. 1986. Laser microprobe mass analysis, Part II. In *Proceedings of the Third International Laser Microprobe Mass Spectrometry Workshop*. Edited by F. Adams and L. van Vaeck. Belgium: University of Antwerp.

Schaufuss, A.G., H.W. Nesbitt, I. Kartio, K. Laajalehto, G.M. Bancroft, and R. Szargan. 1998. Incipient oxidation of fractured pyrite surfaces in air. *J. Electron. Spectrosc. Relat. Phenom.* 96:69–82.

Schaufuss, A.G., H.W. Nesbitt, M.J. Scaini, H. Hochst, G.M. Bancroft, and R. Szargan. 2000. Reactivity of surface sites on fractured arsenopyrite FeAsS toward oxygen. *Am. Mineral.* 85:1754–1766.

Schueler, B.W., R.W. Odom, and C.A. Evans. 1986. Non-resonant multiphoton ionization of neutrals ablated by the laser microprobe technique. In *Proceedings of the Third International Laser Microprobe Mass Spectrometry Workshop*. Edited by F. Adams and L. van Vaeck. Belgium: University of Antwerp.

Senior, G.D., and W.J. Trahar. 1991. The influence of metal hydroxide and collector on the flotation of chalcopyrite. *Int. J. Miner. Process.* 33:321–341.

Shannon, L.K., and W.J. Trahar. 1986. The role of collector in sulfide ore flotation. Pages 408–425 in *Advances in Mineral Processing*. Edited by P. Somasundaran. Littleton, CO: SME.

Shen, Y.R. 1989. Surface properties probed by second-harmonic and sum-frequency generation. *Nature* 337(6207):519.

Simon-Kutscher, J., A. Gericke, and H. Huhnerfuss. 1996. Effect of bivalent Ba, Cu, Ni, and Zn cations on the structure of octadecanoic acid monolayers at the air-water interface as determined by external infrared reflection-absorption spectroscopy. *Langmuir* 12:1027.

Smart, R.St.C. 1991. Surface layers in base metal sulphide flotation. *Miner. Eng.* 4:891–909.

Smart, R.St.C., J. Amarantidis, W.M. Skinner, C.A. Prestidge, L. LaVanier, and S.G. Grano. 2003. Surface analytical studies of oxidation and collector adsorption in sulfide mineral flotation. Pages 3–60 in *Topics in Applied Physics*. Volume 85. Solid-Liquid Interfaces. Edited by K. Wandelt and S. Thurgate. Berlin: Springer-Verlag.

Smart, R.St.C., M. Jasieniak, C. Piantadosi, and W.M. Skinner. 2003. Diagnostic surface analysis in sulfide flotation. Pages 241–248 in *Proceedings, Flotation and Flocculation: From Fundamentals to Applications*, Hawaii, July 28–August 2, 2002. Edited by J. Ralston, J.D. Miller, and J. Rubio. Adelaide: Ian Wark Research Institute, University of South Australia.

Smart, R.St.C., M. Jasieniak, K.E. Prince, and W.M. Skinner. 2000. SIMS studies of oxidation mechanisms and polysulfide formation in reacted sulfide surfaces. *Miner. Eng.* 13:857–870.

Smart, R.St.C., and B. Judd. 1994. Improved Lasta filter and copper reflotation performance through surface analysis surveys at WMC's Olympic Dam operation. Pages 1–4 in *Proceedings of the 5th Mill Operators' Conference*. Melbourne: Australasian Institute of Mining and Metallurgy.

Smart, R.St.C., W.M. Skinner, and A.R. Gerson. 1999. XPS of sulfide mineral surfaces: Metal-deficient, polysulfides, defects and elemental sulfur. *Surf. Interface Anal.* 28:101–105.

Smiley, B.L., and G.L. Richmond. 1999. Alkyl chain ordering of asymmetric phosphatidylcholines adsorbed at a liquid-liquid interface. *J. Phys. Chem. B* 103(4):653.

Sperline, R.P., S. Muralidharan, and H. Freiser. 1987. In situ determination of species adsorbed at a solid-liquid interface by quantitative infrared attenuated total reflectance spectrophotometry. *Langmuir* 3:198.

Stowe, K.G., S.L. Chryssoulis, J.Y. Kim, and C.G. Weisener. 1993. LIMS studies of mineral surfaces in sulphide flotation. Pages 457–460 in *Secondary Ion Mass Spectrometry, SIMS IX*. Edited by A. Benninghoven, Y. Nihei, R. Shimizu, and H.W. Werner. New York: John Wiley & Sons.

Suoninen, E., and K. Laajalehto. 1993. Structure of thiol collector layers on sulfide surfaces. Pages 625–629 in *Proceedings of the XVIII International Mineral Processing Congress*, Sydney, Australia. Volume 3. Melbourne: Australian Institute of Mining and Metallurgy.

Swift, P. 1982. Adventitious carbon—the panacea for energy referencing? *Surf. Interface Anal.* 4:47–51.

Szargan, R., A. Schaufuss, and P. Rossbach. 1999. XPS investigation of chemical states in monolayers: Recent progress in adsorbate redox chemistry on sulphides. *J. Electron. Spectrosc. Rel. Phenom.* 100:357–377.

Taylor, C.J., J.N. Brunt, N. Dixon, and P.J. Gregory. 1978. The application of advanced image analysis techniques. Pages 433–489 in *Proceedings of the Symposium on Quantitative Analysis of Microstructures in Materials Science, Biology and Medicine*. Edited by J.L. Chermant. Stuttgart, Germany: Rieder-Verlag GmbH.

Tejedor-Tejedor, M.I., and M.A. Anderson. 1990. The protonation of phosphate on the surface of goethite as studied by CIR-FTIR and electrophoretic mobility. *Langmuir* 6:602.

Tickanen, L.D., M.I. Tejedor-Tejedor, and M.A. Anderson. 1997. Quantitative characterization of aqueous suspensions using variable-angle ATR-FTIR spectroscopy: Determination of optical constants and absorption coefficient spectra. *Langmuir* 13:4829.

Todd, E.C., and D.M. Sherman. 2003. Surface oxidation of chalcocite Cu_2S under aqueous pH=2–11 and ambient atmospheric conditions: Mineralogy from Cu L-and O K-edge X-ray absorption spectroscopy. *Am. Mineral.* 88:1652–1656.

Trahar, W.J. 1981. A rational interpretation of the role of particle size in flotation. *Int. J. Miner. Process.* 8:289–327.

Uhlig, I., R. Szargan, H.W. Nesbitt, and K. Laajalehto. 2001. Surface states and reactivity of pyrite and marcasite. *Appl. Surf. Sci.* 179:222–229.

van der Steldt, K., W. Skinner, and S. Grano. 1993. A study of the interaction of di-cresyl, dithiophosphate with galena and pyrite using micro flotation, z potential measurements and X-ray photoelectron spectroscopy. Report. Ian Wark Research Institute, University of South Australia.

von Oertzen, G.U., S.L. Harmer, and W.M. Skinner. In press. XPS and *ab initio* calculation of surface states of sulfide minerals: Pyrite, chalcopyrite and molybdenite. *Mol. Simul.*

von Oertzen, G.U., W.M. Skinner, and H.W. Nesbitt. 2005. *Ab initio* and X-ray photoemission spectroscopy study of the bulk and surface electronic structure of pyrite (100) with implications for reactivity. *Phys. Rev. B* 72(235427):1–10

Wang, X. 2004. Ph.D. thesis, Metallurgical Engineering Department, University of Utah, Salt Lake City.

Weisenet, C., and A.R. Gerson. 2000. Cu(II) adsorption mechanism on pyrite: An XAFS and XPS study. *Surf. Interface Anal.* 30:454–458.

Wellham, E.J., L. Elber, and D.S. Yan. 1992. The role of carboxy methyl cellulose in the flotation of a nickel sulfide transition ore. *Min. Eng.* 5:381–395.

Wittstock, G., I. Kartio, D. Hirsch, S. Kunze, and R. Szargan. 1996. Oxidation of galena in acetate buffer investigated by AFM and photoelectron spectroscopy. *Langmuir* 12:5709–5721.

Woods, R., and G.A. Hope. 1998. Spectroelectrochemical investigations of the interaction of ethyl xanthate with copper, silver and gold: I. FT-Raman and NMR spectra of xanthate compounds. *Colloids Surf. A* 137:319–328.

———. 1999. A SERS spectroelectrochemical investigation of the interaction of O-isopropyl-N-ethylthionocarbamate with copper surfaces. *Colloids Surf. A* 146:63–74.

Woods, R., G.A. Hope, and G.M. Brown. 1998a. Spectroelectrochemical investigations of the interaction of ethyl xanthate with copper, silver and gold: II. SERS of xanthate adsorbed on silver and copper surfaces. *Colloids Surf. A* 137:329–337.

———. 1998b. Spectroelectrochemical investigations of the interaction of ethyl xanthate with copper, silver and gold: III. SERS of xanthate adsorbed on gold surfaces. *Colloids Surf. A* 137:339–344.

Woods, R., G.A. Hope, and K. Watling. 2000. A SERS spectroelectrochemical investigation of the interaction of 2 mercaptobenzothiazole with copper, silver and gold surfaces. *J. Appl. Electrochem.* 30:1209–1222.

Young, C.A., and J.D. Miller. 2000. Effect of temperature on oleate adsorption at a calcite surface: An FT-NIR/IRS study and review. *Int. J. Miner. Process.* 58:331.

Zachwieja, J.B., J.J. McCarron, G.W. Walker, and A.N. Buckley. 1989. Correlation between the surface composition and collectorless flotation of chalcopyrite. *J. Colloid Interface Sci.* 132(2):462–468.

Zhu, X.D., H. Suhr, and Y.R. Shen. 1987. Surface vibrational spectroscopy by infrared-visible sum frequency generation. *Phys. Rev. B* 35(6):3047.